Aalto University
School of Science
Master's Programme in Engineering Physics

Sukanta Datta

High-yield preparation of transparent films with large-diameter CNTs via FCCVD

Master's Thesis

Espoo, December 10, 2019

Supervisor: Professor Esko I. Kauppinen

Thesis advisor(s): Dr. Qiang Zhang

AALTO UNIVERSITY
School of Science
Master's Programme in Engineering Physics

ABSTRACT OF THE
MASTER'S THESIS

Author Sukanta Datta

Title of thesis High-yield preparation of transparent films with large-diameter CNTs via FCCVD

Master programme Engineering Physics

Thesis supervisor Esko I. Kauppinen

Thesis advisor(s) Qiang Zhang

Date 10.12.2019 **Number of pages** 43 **Language** English

Abstract

Carbon nanotube (CNT) thin films are the promising material to replace indium tin oxide for the applications in transparent and conductive electronics. We report the synthesis of high-yield CNTs with CH_4 as carbon source via floating catalyst chemical vapor deposition (FC-CVD) system. With the optimized synthesis parameters, CNT TCFs have a sheet resistance of 59 Ω/sq at 90 T% with 10 min collection on a 4.7 cm diameter filter. Here, the yield of CH_4-based CNT film is much higher than those of other SWCNT films, e.g. 20 times of CO-based single-walled carbon nanotube (SWCNT) films with 86.8 Ω/sq at 90 T%, 150 times of C_2H_4-based SWCNT films with 51 Ω/sq at 90 T% and 10 times of C_2H_6O-based SWCNT films with 78 Ω/sq at 90 T%. Moreover, we applied TEM and SEM to analyze the morphology of CNTs. Surprisingly, double-walled carbon nanotubes (DWCNTs) with the proportion up to 80% were found. These DWCNTs with a diameter of 3.5-6 nm constitute into bundles with a mean diameter of 8.3 nm and a mean length of 14.52 μm. We believe these DWCNTs with unique morphology contribute to high-performance CNT TCFs with high yield.

Keywords Carbon nanotube; single-walled carbon nanotube; floating catalyst chemical vapor deposition; transparent conductive film

Acknowledgements

The research work in this thesis was carried out from February 2019 to August 2019 at the Department of Applied Physics, Aalto University School of Science. During which I have received lots of support and many people deserve my thanks. First of all, I would like to thank my supervisor professor Esko I. Kauppinen, for accepting and funding me as a master's thesis student in Nanomaterials Group. His supervision on my research not only let me see the big picture, but also the details and fundamentals. His attitude of keeping learning and being curious about new knowledge always inspires me. In addition, I wish to thank my thesis advisor, Dr. Qiang Zhang. Qiang's experience in synthesis also helps me find better solutions to improve the reactor's stability and synthesize the desired samples. I greatly benefited from Qiang's deep understanding of the nanocarbon materials.

The time of working in the lab together with my colleagues was unforgettable, so I wish to thank my group members Er-Xiong Ding, Yongping Liao, Saeed Ahmad, Nurul Huda, Aqeel Hussain, Taher Khan, Dr. Hua Jiang, Dr. Nan Wei, and Dr. Mohammad Tavakkoli. We worked together to build or modify a reactor and discuss the problems we met and find the solutions in the lab. Without your contributions, this thesis work can hardly go so smoothly.

I thank my parents and my siblings for their infinite love and support for me during my whole life.

Espoo, December 10th, 2019

Sukanta Datta

Contents

1. Introduction

Carbon nanotubes (CNTs), particularly single walled carbon nanotubes (SWCNTs), have become a point of discussion during the last two decades. Since the discovery by Iijima in 1991, SWCNT has drawn great interest to be used as a promising material owing to its unique chemical and physical properties that make them useful for wide applications [1,2]. Specifically, the CNT-based thin films have vast applications in transparent conductive films (TCFs) and thin film transistors (TFTs) [3,4]. TCFs are optically transparent and electrically conductive materials, which are widely used in electronics applications, *e.g.* flat panel displays, touch sensors and photovoltaics [5]. Indium tin oxide (ITO) currently is the dominant material for industrial-scale TCF application as it has outstanding properties with a sheet resistance of 10 Ω/sq at 90% optical transmittance [6]. However, the poor mechanical stability, high refractive index and limited supply of ITO have prevented many challenges for the development of future electronics. Importantly, as a brittle ceramic, the brittle nature of ITO hinders its sustainable application in future optoelectronics which need mechanically flexible, lightweight and low fabrication cost TCF materials. CNT thin film is a promising material that can show high electrical conductivity and high optical transparency. CNT based TCF materials have the potential to replace ITO as they can enable to fabrication process easier as well as provide more stretchable and flexible flatform with stronger mechanical strength. Recently, many companies are attempting to introduce CNTs to upgrade their products. Due to the rapid growth and development of customer electronics, TCFs are a very extensive field for CNTs. The properties of CNTs are highly depended on their morphology and atomic structure, which is becoming a prime challenge to the applications of carbon nanotubes.

Over the last decades, researchers have established a series of techniques of producing CNTs, such as arc discharge [7], laser ablation [8] and chemical vapor deposition (CVD) [9]. Specifically, the floating catalyst CVD (FC-CVD) [10–12], is a continuous process for CNTs synthesis with high yield and quality. FC-CVD has been greatly used in both academic and industrial fields. In our group, earlier researchers reported that the gas-phase CNTs from FCCVD can be directly deposited into the transparent conductive films (TCFs). With optimized conditions, the SWCNT films via FCCVD with CO [13], C_2H_4 [14]or C_2H_6O[15] can have a sheet resistance less than 100 Ω/sq with 90% T, which have been applied in the commercial products. However, there are still many challenges for the industry application of CNT TCFs, especially to further improvement of the conductivity and yield of CNT films.

In this study, the high-quality CNT based films are synthesized via the FC-CVD system with high yield. Methane (CH_4) is used as a carbon source due to the most stable hydrocarbon which means we can produce clean nanotube with a low amount of amorphous carbon at high synthesis temperature. Hydrogen (H_2) and nitrogen (N_2) are applied as carrier gases, ferrocene ($FeCp_2$) as catalyst precursor, and sulfur (S) as a promoter for CNT synthesis. Firstly, the synthesis parameters with a fixed $FeCp_2$ amount were optimized to improve the yield and optoelectronic performance of CNT TCFs. As a result, the CNT TCFs with a low sheet resistance of 75 Ω/sq at 90 T% was obtained with a super-high yield of 4 min collection on a 4.7 cm diameter filter.

To further improve the optoelectronic performance of TCFs, we reduced the CNT yield in a reasonable range via tuning the feeding rate of $FeCp_2$. With the yield decrease, the CNT TCFs performance first improved and then declined. Specifically, CNT TCFs have a sheet resistance of 59 Ω/sq at 90 T% with 10 min collection on a 4.7 cm diameter filter. Here, the yield of CH_4-based CNT film is much higher than those of other SWCNT films, e.g. 20 times of CO-based SWCNT films with 86.8 Ω/sq at 90 T% [13], 150 times of C_2H_4-based SWCNT films with 51 Ω/sq at 90 T% [14] and 10 times of C_2H_6O-based SWCNT films with 78 Ω/sq at 90 T% [15]. Moreover, we applied TEM and SEM to analyze the morphology of CNTs. Surprisingly, DWCNTs with the proportion up to 80% were found. These DWCNTs with a diameter of 3.5-6 nm constitute into bundles with a mean diameter of 8.3 nm and a mean length of 14.52 μm. We believe these DWCNTs with unique morphology contribute to high-performance CNT TCFs with high yield.

2. Background

2.1. Structural properties of SWCNTs

SWCNT is one of the low-dimensional carbon allotropes families which have outstanding geometrical and electronic properties. As shown in Figure 2.1.1, SWCNT is represented as a graphene sheet that is rolled up into 1-dimensional hollow cylindrical shape. Graphene is a hexagonally arranged 2-dimensional carbon crystal structure. In graphene, carbon is formed as sp^2 orbital hexagonal lattice where 2s, $2p_x$, and $2p_y$ formed with the angle of 120° each other. The length of SWCNT varies from tens of nanometers to hundreds of millimeters, and the diameter from sub-nanometer to few nanometers. The carbon atom of SWCNTs forms strong σ bond with their corresponding carbon atom by a sp^2 orbital hybridization, and the continuing p_z orbital forms a π bond with another p_z of its neighbor carbon atom [16]. The SWCNTs unique electrical and mechanical properties can be determined by these π and σ bonds [17].

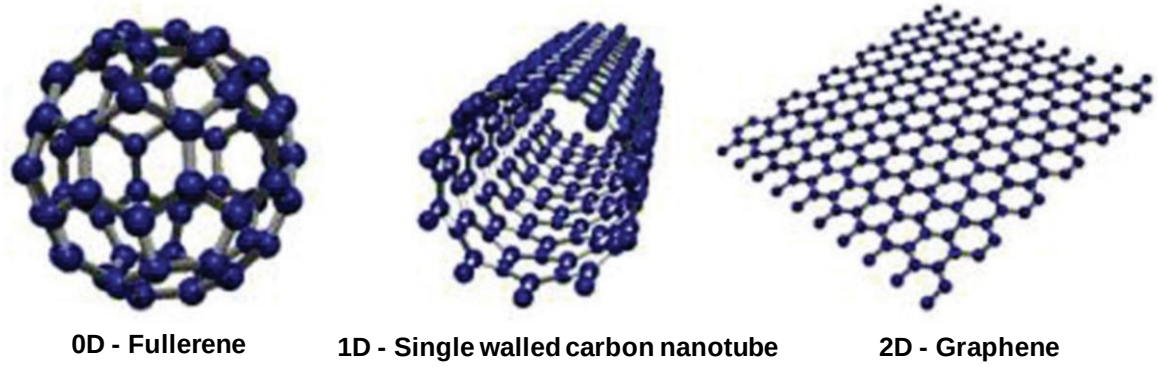

Figure 2.1.1. Schematic representation of the carbon allotropes; Zero-dimensional (0D) fullerene, one-dimensional (1D) single-walled carbon nanotube, and two-dimensional (2D) monolayer graphene. Adapted from [18].

The properties of SWCNT rely on its structure. The SWCNT structure can be expressed by using the graphene unit cell-based vectors a_1 and a_2 determining the chiral vector C_h, which is connected with the two equivalent points on a 2D graphene sheet. The unit vectors are joined if the graphene ribbon is rolled into a tubular SWCNT structure as

$$C_h = na_1 + ma_2 \qquad (2.1.1)$$

The nanotube structure is defined by using the integers (n, m) which are specifying the chiral vector C_h (Figure 2.1.2). The SWCNT structure is categorized as armchair, zigzag or chiral based on the rolling of graphene sheet which is determined by chirality (n, m). For instance, if n is equal to m then SWCNT is classified as armchair. The armchair nanotubes have a metallic band structure. For this structure, the chiral angle θ reaches its maximum at 30° [19]. On the other hand, when m=0, the SWCNT is characterized as zigzag tubes and the chiral angle θ becomes zero. The armchair and zigzag tubes are considered as achiral tubes as their planes are the mirror to each other. The SWCNTs other than achiral are chiral and their chiral angles are in the range between $0 < \theta < 30°$. The chiral angle of SWCNTs is expressed as

$$\theta = \tan^{-1}\left[\frac{\sqrt{3}\,n}{(2m+n)}\right] \qquad (2.1.2)$$

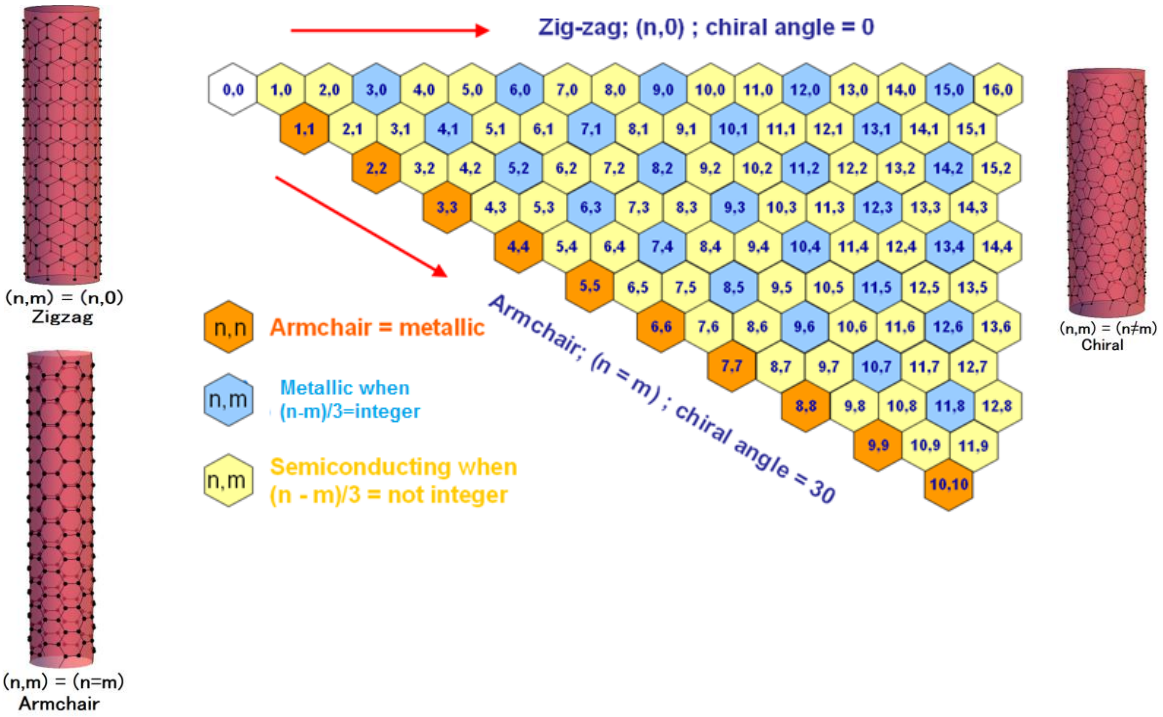

Figure 2.1.2. A graphic displaying a chirality map that defines the carbon nanotubes structure into zigzag, armchair and chiral SWCNTs. Where armchair (n=m) and zigzag (n=0) are the two nanotubes classified at chiral angels of 30° and 0°. Other carbon nanotube types between these limiting cases are categorized as chiral nanotubes.

2.2. Electronic properties of SWCNTs

The electronic properties of SWCNTs can be studied based on the graphene. The electronic transitions in graphene are occurring between the valence and conduction bands. Rolling a graphene sheet, the band structure of SWCNTs can be explained by the tight-binding model with the nearest neighbour interaction [20]. The electron energy dispersion in graphene is given [21],

$$E_{2D}(k_x k_y) = \pm\gamma_0 \left[1 + 4\cos\left(\frac{\sqrt{3}k_x a}{2}\right)\cos\left(\frac{k_y a}{2}\right) 4\cos^2\left(\frac{k_y a}{2}\right)\right] \qquad (2.2.1)$$

where $k_{x,}k_y$ are the wave vectors, γ_0 is the nearest neighbour transfer integral and = 0.246 nm is the in-plane lattice constant.

The electronic properties of SWCNTs can be determined by their structure. As shown in Figure 2.2.1, the Brillion zone of the hexagonal graphene includes corner points indicate the K points. It can be seen that the conduction and valence band meet at the K points which makes a single electronic state at the Fermi level. Thus, graphene is acting as metallic in nature with a zero band gap [20].

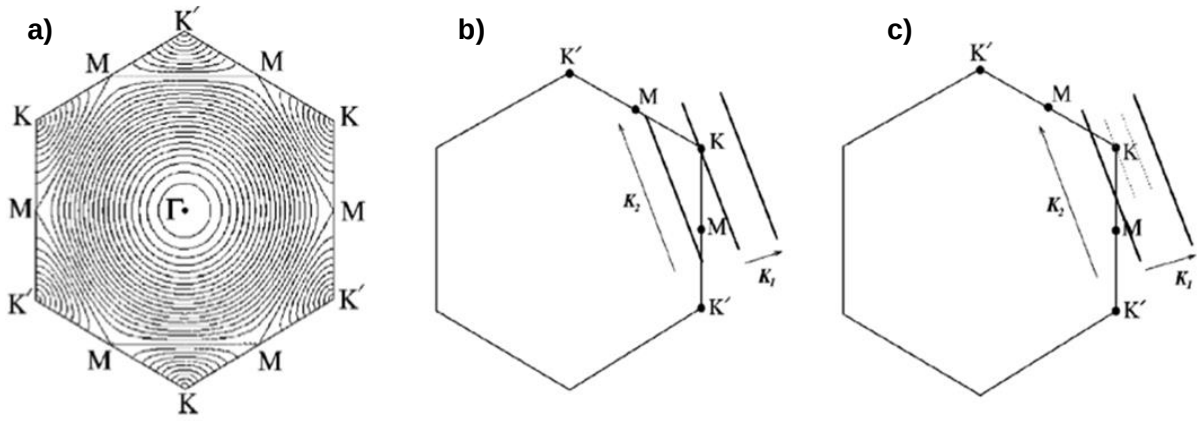

Figure 2.2.1. a) The Brillion zones of graphene, b) metallic CNTs, the bold line intersects a K point at the Fermi level and c) semi-conducting SWCNTs, the bold line does not go through a K point, with a finite energy gap. Adapted with permission from [20].

However, the situation is complicated for the case of SWCNTs . The 2D graphene nanosheet is rolled up into 1D nanotube which induces changes in the electronic structure of SWCNTs. To calculate the allowed 1D subbands, the radial confinement boundary conditions are applied as the following formula

$$C_h * k = 2\pi \mathrm{p} \qquad (2.2.2)$$

where C_h is the chiral vector and p is an integer.

The nanotube is called metallic SWCNTs if any of the 1D subbands passes through the k point. Otherwise, it is known as semiconducting CNTs [16]. For example, for metallic CNTs (n-m)/3 = integer where subband meets at the K point with creates an electronic state at Fermi level (Figure 2.2.1b) [22,23]. Therefore, it represents the metallic behavior of SWCNTs with a zero band gap. However, for (n-m)/3≠ integer, the allowed subband does not touch at the corner points of the 1st Brillion zone [23]. Thus, it is referred to as the semiconducting nature of SWCNTs. As there is no density of state at the K point in the case of semiconducting SWCNTs, the band gap is inversely proportional to the diameter of the tubes.

2.3. Optical properties of SWCNTs

The optical absorption spectrum (OAS) of CNTs can be used to measure the absorption of electromagnetic radiation in a sample over the function of the wavelength. When the light propagates through an absorbing medium, its intensity decreases exponentially. The relationship between the incident and transmitted light can be expressed by according to Beer-lambert formula:

$$I(L) = I_0 e^{-\alpha L c} \qquad (2.3.1)$$

where the intensity of transmitted light is I (L), I_0 is the intensity of incident light, the absorption coefficient is α, L is the optical path length, and c is the concentration of absorbing species in the material. As shows in Figure 2.3.1, by measuring the transmitted intensity with respect to the incident intensity. However, the absorbance can be expressed by the following equation:

$$A = -\ln(\tfrac{I}{I_0}) \qquad (2.3.2)$$

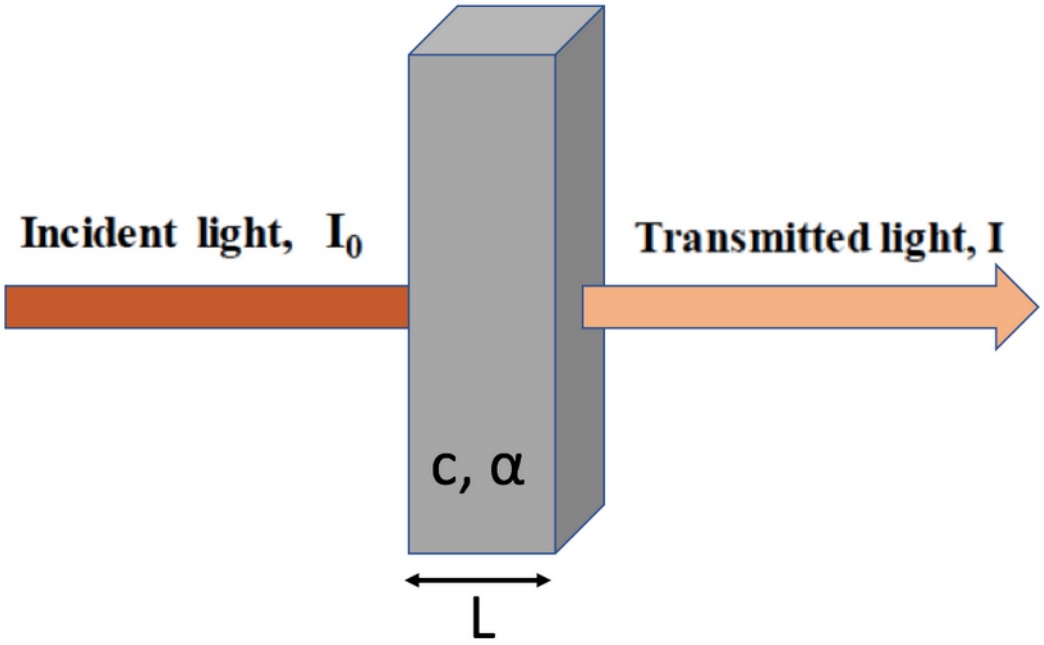

Figure 2.3.1. The optical absorption in material including concentration of absorption species c and absorption coefficient α. The optical path length is L, and the incident and transmitted intensities are I and I_0, respectively.

The OAS is a reliable technique for understanding nanotubes characterization. Optical absorption spectra are typically used to determine the diameter of SWCNTs by scanning a sample in ultraviolet- visible and near-infrared (UV-VIS-NIR) region of the spectrum. The optical response of SWCNTs consists of electronic transitions occurring between valence and conduction bands. These transitions are known as van hove singularities.

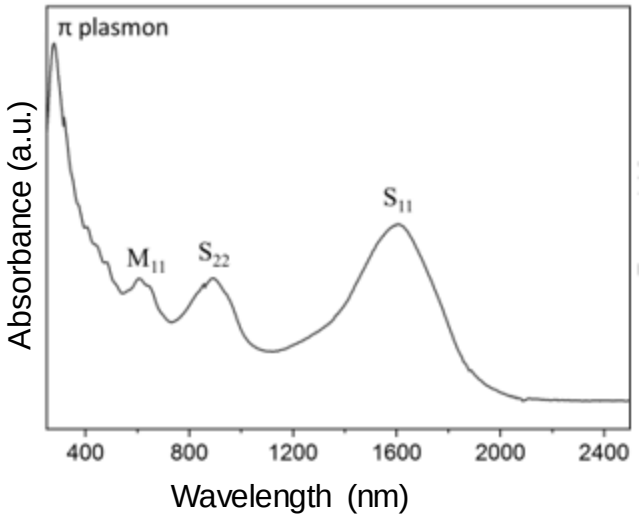

Figure 2.3.2. The typical optical spectrum of a CNT thin film. Image adapted from [24].

For the nanotube characterization, the corresponding wavelength typically ranges from 200 nm up to 2600 nm. As depicted in Figure 2.3.2, a typical absorption spectrum of SWCNTs consists of three absorption peaks, which are associated with the first optical transition in metallic tubes

depicted as $M_{11,}$ first transition in semiconducting tubes as S_{11}, and second transition in semiconducting tubes as S_{22}. The relationship of optical transitions of CNTs is inversely proportional to the nanotube diameter [25]. According to the tight-binding model, the optical transition energy can be formulated:

For semiconducting SWCNTs $E_{11}^{S} = \frac{2a_0\ \gamma_0}{d}$ (2.3.3)

$E_{22}^{S} = \frac{4a_0\ \gamma_0}{d}$ (2.3.4)

For metallic SWCNTs $E_{11}^{M} = \frac{6\ a_0\ \gamma_0}{d}$ (2.3.5)

where γ_0 is the nearest-neighbor transfer integral.

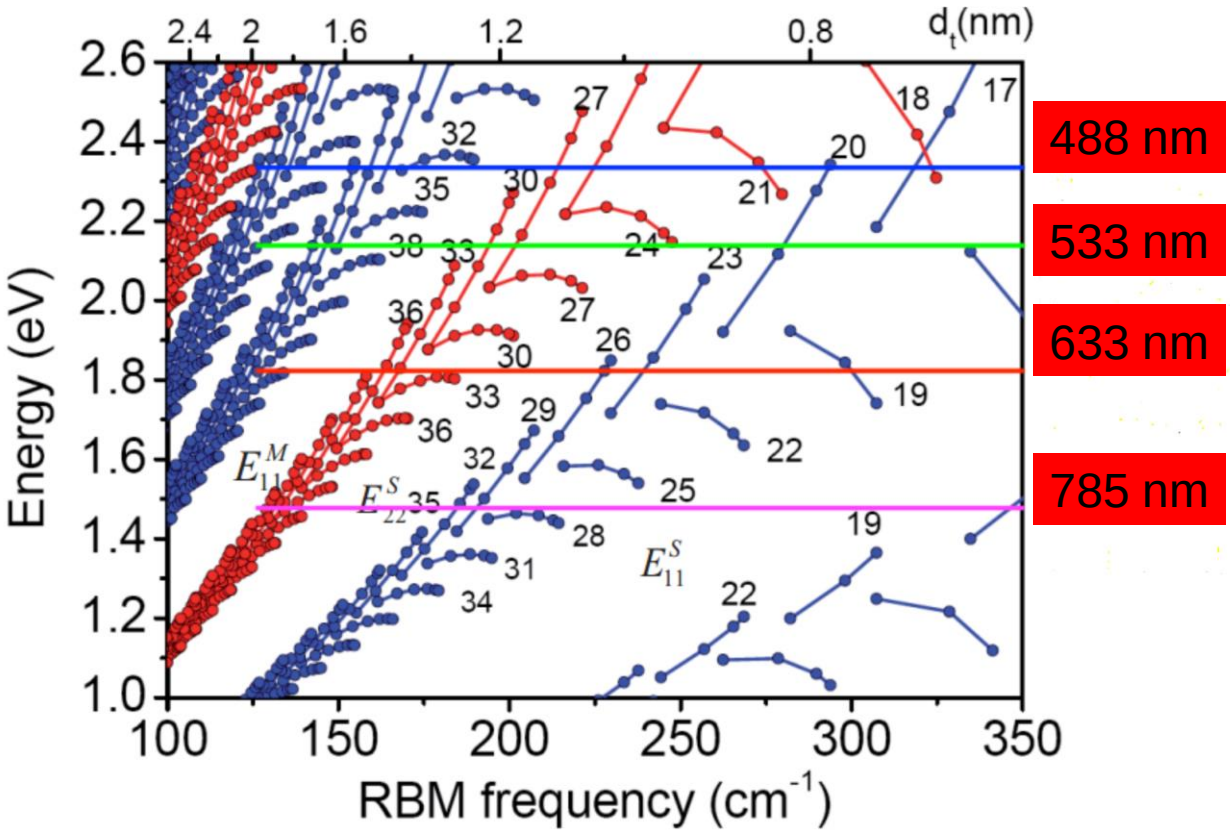

Figure 2.3.3. A schematic illustrating the Kataura plot for optical transitions, the blue branches referred to the transitions of s-CNT, and the red branch associated with the transitions of m-CNT. According to this plot, we can estimate the mean diameter of CNTs based on the transition energies.

However, the effect of curvature, the c-c bond length optimization, and many-body effects are not included in the tight binding model. A Kataura plot depicted in Figure 2.3.3, which shows the relationship between transition energy and tube diameter. The approximate mean diameter of CNTs in a thin film sample can be determined based on the peak positions. Aside from the electronic transition peaks, there is a strong-intensity π plasmon absorption peak can also be detected, which attributes to the collective oscillation of π electrons in carbon as well as other impurities inside the sample [26].

Raman scattering is another vital optical phenomenon, which is exhibited by CNTs and Raman

spectroscopy is a widely used technique for their characterization. Raman scattering is the inelastic scattering of the incident photon from molecules. This scattering classified as stokes and anti-stokes scattering. The emission of phonon is referred to as stoke scattering and anti-stoke scattering is associated with the absorption of phonon.

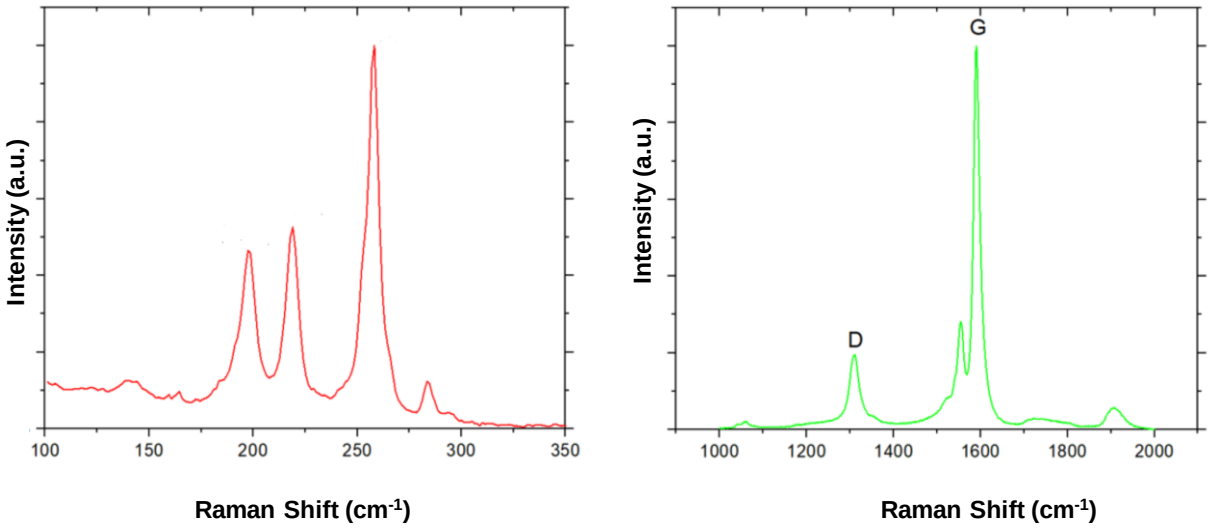

Figure 2.3.4. A typical Raman spectrum from a CNT thin film sample excited by a 633 nm laser.

As shown in Figure 2.3.4, a typical Raman spectrum of CNTs with the two important features defined as radial breathing mode (RBM) and tangential mode (the G and D bands). In the case of RBM, the out-of-plane vibrations oriented radially away from the CNT axis. Thus, the diameter of the entire CNT oscillates like breathing (Figure 2.3.5a). The RBM peaks appear in the lowest energy region between the frequency range region 100-400 cm^{-1}.

In principle, a single RBM peak illustrates only a single type of tube in the sample or RBM peaks from various resonant CNTs. The RBM peaks are used to determine the SWCNT diameter and chirality (n, m) based on the Kataura plot (Figure 2.3.3) and each point in Kataura plot shows one (n, m) of CNT. The relationship between the diameter (d_t) of CNTs and the RBM frequency (ω_{RBM}) is used to determine the diameter of the nanotubes. This formula is expressed as

$$\omega_{RBM} = \frac{A}{d_t} + B \qquad (2.3.6)$$

where A = 217.8 and B = 15.7 are experimentally calculated values [27,28].

The prime limitation of the Raman is that the RBM peaks can not appear for all the nanotubes. However, only nanotubes that are in resonance show RBM peaks and their diameter can only be measured correspondingly. Thus, it is very hard to find the diameter distribution of all the nanotubes those are appeared in the sample using Raman spectroscopy.

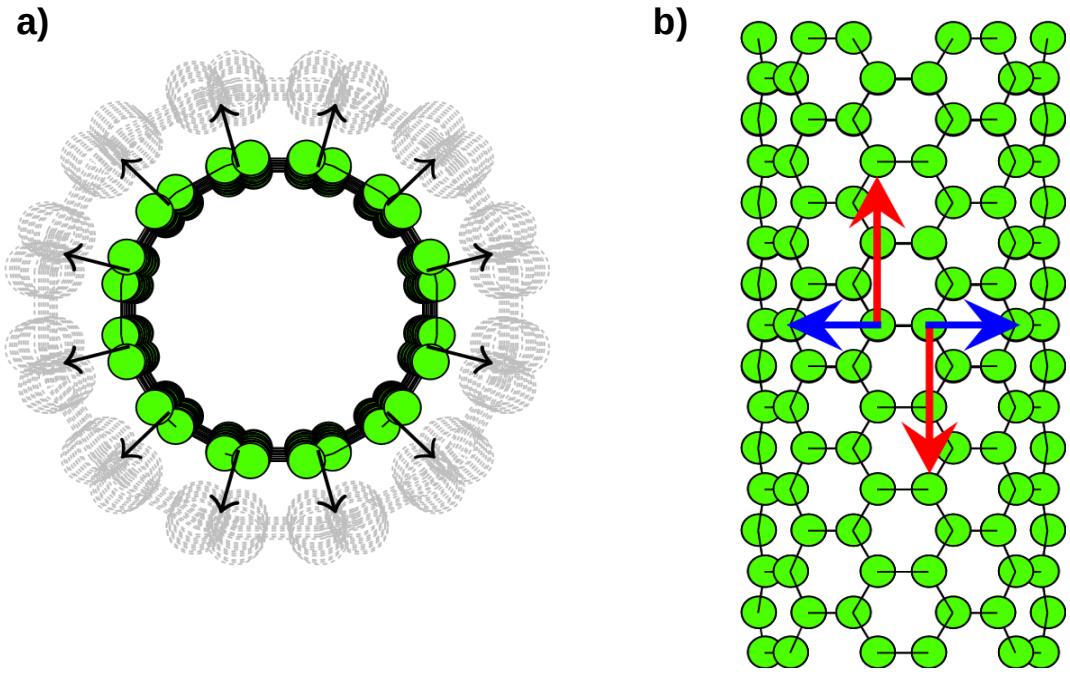

Figure 2.3.5. Schematic illustrates the vibration modes excitation in Raman spectra a) The out-of-plane vibration which is associated to increase the radial breathing mode excitations. b) The in-plane vibrational modes which are corresponding to the G band Raman signal. Image adapted from [29].

In Raman spectra, the dominant peak appears at ~1590 cm^{-1} is called the G band which refers to the graphite-like band. As can be seen from Figure 2.3.5b, this band is phonon mode between a pair of carbon atoms in the graphene unit cell and there is a vibration that happened tangentially in between two carbon atoms [30]. Owing to the curvature, the G band of CNTs splits into two energy peaks, such as lower energy G^- (~1570 cm^{-1}), and higher energy G^+ peak (~1590 cm^{-1}). Interestingly, the G^+ peak is associated with the lattice vibration in the CNT axis direction, and the G^- peak vibrates along the circumferential direction. Thus, it is very difficult to identify whether the nanotube is semiconducting or metallic from the G^- peak. In addition to the G band, the peak appears at ~1350 cm^{-1} is called D band which indicates that the disordered properties caused by the vacancies, or any defects. Notably, the intensity ratio of G/D is commonly used to evaluate the structural quality of CNTs.

2.4. Synthesis of CNTs

2.4.1. Different techniques for CNTs

Currently, there are three most common methods to prepare CNTs (Figure 3.1.1), consists of arc discharge, laser ablation and chemical vapor deposition (CVD). The CVD is further divided into substrate chemical vapor deposition (S-CVD) and floating catalyst chemical vapor deposition (FCCVD) method.

Since the discovery in 1991, the arc discharge is the first method to produce carbon nanotubes developed by Iijima [1]. In this method, high temperature (over 1700 °C) is required for CNT growth. The two electrodes having a distance (1-2 mm) are placed in a vacuum chamber filled with helium or argon as an inert gas (Figure 2.4.1a). If the electric current passes through the positive and negative electrodes then the high temperature can turn the gas into plasma and evaporate the electrode materials with charged nanoparticles. In arc discharge, usually the

electrodes are made of graphite. The evaporated anode carbon will be deposited on the cathode surface.

The researchers have found that the CNTs wall number relies on the composition of electrodes. Thus, the metal-doped graphite electrodes will lead to the SWCNTs and the pure graphite electrodes to MWCNTs. It has been proven that the metal-doped graphite is more effective to control the diameter of SWCNTs. For example, Bethune *et al.* [31] and Ajayan *et al.*[32] investigated the composition of carbon and cobalt regarding the synthesis of the very small diameter of CNT (1.2 nm). Moreover, catalyst-doped graphite has also been studied such as Fe, Ni, and platinum-group metals [33–37].

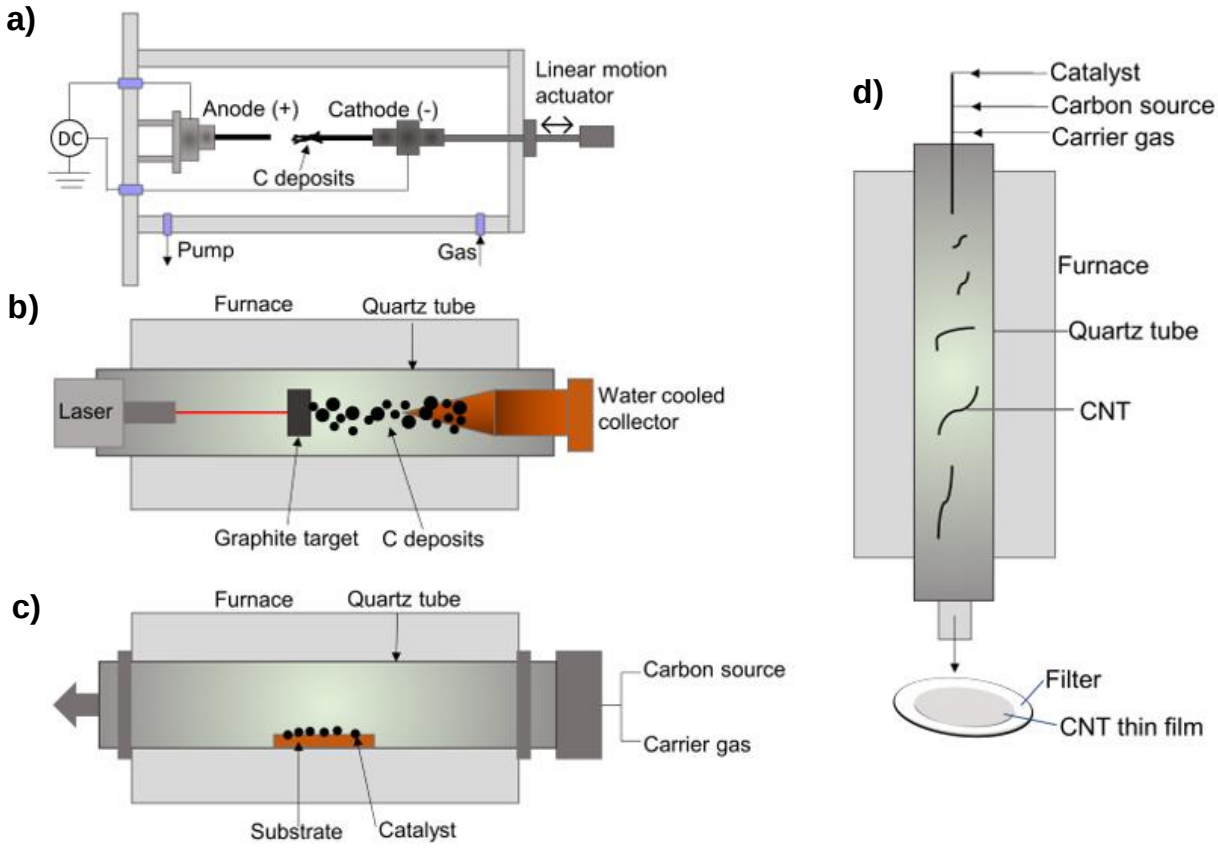

Figure 2.4.1. Schematics of various techniques for carbon nanotube synthesis. (a) Arc discharge, (b) Laser ablation, (c) substrate chemical vapor deposition, adapted from [24], and (d) floating catalyst chemical vapor deposition, which is used in this thesis.

The laser ablation technique for SWCNT synthesis was firstly established by Smalley *et al.* in 1995 [8] (Figure 2.4.1b). The mechanism of this method is similar to arc discharge, but a laser beam is utilized for the evaporation of graphite. In this technique, high temperature is used in furnace for the SWCNT growth and the furnace is filled with the inert gas. The metal or graphite target is bombarded by using a laser. After that, the vaporized carbon and metal particles will be reconstructed into the form of carbon nanotubes, and the generated CNTs are then deposited on a cooled surface. Researchers have reported that the laser source [38] and transition metal composition [39,40] will have a promising effect on the CNT growth.

In general, these two methods (arc discharge, laser ablation) are very practical methods for CNT synthesis as they can yield highly graphitized nanotubes with high temperatures. However, the high synthesis temperature leads to a big challenge for large-scale production of CNTs. Moreover, by-products appear along with the SWCNTs, such as MWCNTs, amorphous carbon

and metallic particles. Therefore, further treatment is a prerequisite to achieve high-purity SWCNTs. It is also very hard to control the chirality of SWCNTs using these two methods.

On the other hand, Chemical vapor deposition (CVD), has taken into account as the most widely used procedure for large-scale production of SWCNTs with high quality and selectivity. In 1996, the growth of CNTs using the CVD method was first developed by Dai *et al.* [9]. In general, the carbon source which decomposes on the catalyst surface at high temperature or plasma, and then start to grow SWCNTs. Recently, two growth models named the tip growth [41] and base growth [42], are generally accepted through the actual growth mechanism remains elusive. On the basis of how catalyst is produced, we separate the CVD method into two categories, the substrate CVD (S-CVD, Figure 2.4.1c), where the catalysts are spread on the surface of substrate, and the floating catalyst CVD (FC-CVD, Figure 2.4.1d), where the catalysts are carried by gas into the furnace.

In S-CVD, the transition metals (Fe, Co, Ni, etc.) are deposited on the substrate and carbon precursor is catalytically decomposed in the presence of high-temperature furnace (700-1200 ^{o}C). This S-CVD method is essential for preparing the horizontally aligned CNTs [43] and the CNT forest [44]. On the other hand, based on the catalyst activity and substrate size the S-CVD large-scale production is limited.

Importantly, FC-CVD, a scalable and continuous process compared to arc discharge and laser ablation or S-CVD methods. FCCVD, is the method which is more convenient and controllable [45], is an effective process to large-scale production of CNTs with high quality [46] as well as enable to direct synthesis of various SWCNT architectures, as for example transparent films [47,48], continuous fibers [49,50], and CNT sponges [51].

There are several features of FC-CVD can affect the morphology and properties of the CNTs, with catalyst decomposition, catalyst size, temperature, carbon source, and gas-phase chemistry being the five principle parameters [52,53]. In FC-CVD, the most productive catalysts are formed from pyrolysis of sublimed organometallic compounds, such as carbonyl iron, ferrocene, dimethoate, or metal nanoparticles generated using a hot-wire or spark system [54–56]. In 1998, Cheng *et al*. first established the FC-CVD method to synthesize SWCNTs where ferrocene was used as a catalyst [12,57]. Therefore, the result of this work reported that FC-CVD is a great potential method for high yield production of CNTs. The diameter of the nucleated CNTs is slightly smaller than the size of the catalyst. There are many outstanding carbon sources for the growth of CNTs are known, such as hydrocarbons and carbon monoxide (CO) [53]. In general, hydrocarbons are thermally self-decomposed into carbon clusters ($C_x H_y$) and then they are absorbed by the catalyst. Thus, this approach can enable to produce the fast and high yield growth of CNTs [58]. In contrast, the production of amorphous carbon might increase with the increase of partial pressure of the hydrocarbon or temperature. The CO as a carbon source is notably different from hydrocarbons. It decomposes at the surface of the catalyst nanoparticles, generating carbon atoms for CNT formation, while the disproportionation reaction needs the existence of a catalyst surface [59].

$$2CO \leftrightarrow C\ (s) + CO_2\ (g) \qquad (2.4.1)$$

This reaction can immensely decrease by-product generation. The growth of SWCNT with the CO disproportionation has been taken at either high or atmospheric pressure (Figure 2.4.2), and both methods have the large-scale applications on commercial production of SWCNTs and films.

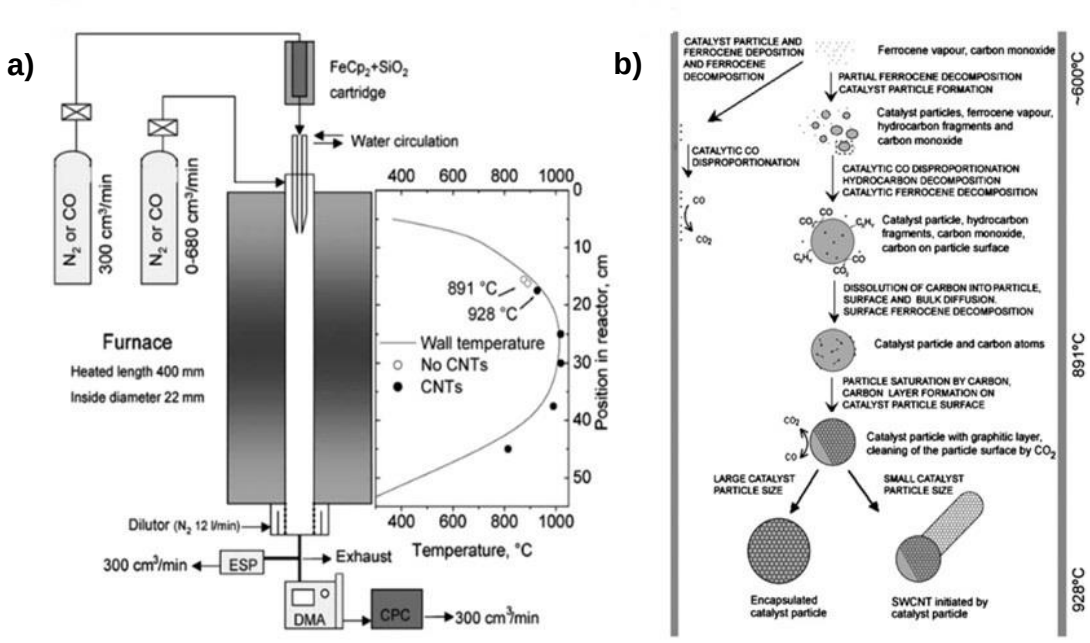

Figure 2.4.2. Synthesis of high-quality CNTs with CO as a carbon source at atmospheric pressure based on FCCVD [11]. a) The schematic represents the experimental setup and wall temperature profile for FCCVD synthesis of CNTs with ferrocene as a catalyst. Open circles indicate sampling locations where CNTs were not observed and solid circles refers to the conditions for CNT sampling. b) The diagram of the CNT formation mechanism in the $FeCp_2$–CO system at a temperature of 1000 °C.

In 2001, another FC-CVD procedure was developed by Smalley *et al.* [46] where the CO used as a carbon source at high pressure which is known as the HiPco SWCNTs, to produce large-scale production of SWCNTs with the presence of iron nanoparticles formed from the decomposition of iron pentacarbonyl. Currently, He *et al.* [60] and Koziol *et al.* [53] reported that the structural distinguishes between tubes grown using CO, methane, ethanol, toluene by electron diffraction methods. The optimal growth temperature for CNT formation appeared to range from 700 to 1200 °C. Argon, helium, nitrogen or hydrogen are very commonly used carrier gas for feedstock introduction and product carriage, but enough research has not been carried out on the difference between using helium, argon or nitrogen for the CNT growth. Notably, one study suggests that when the flow rates of hydrogen increase then the decomposition of hydrocarbons decreases. Thus, iron oxide can be reduced during the production of CNTs [61,62]. Moreover, hydrogen can etch CNTs and amorphous carbon.

After that, Kauppinen *et al*. established the FC-CVD method to obtain high-quality, high-yield SWCNTs where SWCNTs can be produced in ambient pressure using CO as carbon source [11,54,55,63]. As shown in Figure 2.4.2a, the laminar reactor for SWNT production with a water-cooled injector and a vertical furnace. The injector probe reaches into the high-temperature zone of the vertical CVD reactor. Recirculation of the extra flow occurs only in the region close to the injector probe outlet. However, the flow of the nanoparticles does not take part in the recirculation, the total flow becomes fully established and laminar as it moves towards the high temperature zone of the furnace, specifying laminar flow conditions for catalyst particle formation and SWNT growth. The aerosol of catalyst or precursor, carbon source, and carrier gas are introduced via an injector probe into the high temperature zone of the vertical CVD reactor. In the reactor end, the floating CNTs and bundles can be directly and continuously obtained.

The schematic of catalyst formation and SWCNT growth process in FC-CVD where CO as carbon source and $FeCp_2$ as catalyst precursor is in Figure 2.4.2b. Decomposition of $FeCp_2$ vapor results in catalyst particle formation and then carbon source also decomposes and add to the catalyst. Catalyst particles are then formed by nucleation and continue to grow via collision processes. Moreover, the disproportionation of CO molecule takes place on the nanoparticle surface until saturation. The time limit of SWCNT growth might be determined by the dynamic temperature zone in the reactor and the inactivity of catalyst due to their size or excess saturation, as well as the bundling because of the collision between the SWCNTs. Moreover, the CNT growth window for temperature for the CO system was estimated to be 891 to 928 ^{o}C [11].

FC-CVD method has drawn great attention in the academic filed. In this method, the SWCNT parameters can be controlled by modulating the reactor and applying various feeding conditions. For instance, the bundle diameter of SWCNTs can be modulated by controlling the catalyst flowing rate [64], and the bundle length of SWCNTs can be increased by scaling up the reactor dimension [48].

Apart from the fundamental research, FC-CVD method has been considered as a promising process for the industry standard large-scale production of SWCNTs because of continuous feeding of carbon source and catalysts. At present, the industrial production of CNT thin films has produced by FC-CVD method and having a great potential to replace the conventional indium tin oxide (ITO) materials.

3. Transparent Conductive Films

Transparent conductive films (TCFs), which are electrically conductive and optically transparent material. TCFs have drawn attention due to their various applications in modern technology, such as solar cells, touch panels, liquid crystal displays (LCD) or organic light-emitting diodes (OLED) [65]. The TCF displays with low sheet resistance (R_s) at high light transmittance (T), where T is measured from optical absorption spectroscopy and R_s is measured by the four-probe method. We can add these two parameters to define the figure of merit K of TCFs as follows in,

$$K = (R_s \times lnT)^{-1} \tag{3.1}$$

where higher K value provides the better performance of TCFs.

Nowadays, indium tin oxide (ITO) is widely used material for industry-standard role TCF application as it has low sheet resistance (from 10 to 100 Ω/sq) at high light transmittance (>85%) [66,67]. However, ITO is fragile [68] and the indium element reservation is very low [69]. Because of these drawbacks, it has limited its further application for flexible TCFs in the future. Therefore, it has been motivating the look for new alternative TCF materials. Researchers have found several materials with great potential instead of ITO, such as silver nanowires [70–72], copper nanowires [6], graphene [73,74] and SWCNTs [3,75,76].

Owing to high conductivity, the silver nanowires (Ag NWs) based TCF with the sheet resistance of 20 Ω/sq at 95% transmittance, which is better than ITO. However, the limitations of silver nanowires are the high cost of raw materials, the oxidation in air and the reflection increases with wavelength. As copper is cheaper than silver, copper nanowires (Cu NWs) are also becoming the most promising materials in TCF technology. Although Cu NWs can obtain the best TCFs with a sheet resistance of 100 Ω/sq at 95% transmittance, the stability of Cu NWs against oxidization is a big challenge [6].

Graphene has a very good optical and electrical properties and it can be used as an ideal material for TCF application. But, the electrical properties greatly rely on graphene quality. With the four or five layers of mechanically exfoliated graphene TCF exhibits very low sheet resistance of 8.8 Ω/sq at 84% transmittance [73,77,78]. The solution process based graphene TCF illustrates a sheet resistance of above 1000 Ω/sq at 85% transmittance [79–82]. However, the defects (grain boundary, wrinkles, folds or cracks) and the transfer difficulties are the main problems of graphene for TCF application.

However, SWCNT is becoming a promising material for TCF applications because of its easy production, super electrical conductivity, flexibility and good chemical stability.

3.1. Transparent conductive SWCNT films

The SWCNT films are formed from continuous network of nanotubes or bundles of nanotubes. As depicted in Figure 3.1.1a, a scanning electron microscopy image of SWCNT network and its implementation as transparent conductive film on PET from Ding *et al.* [15] Since the film is very thin such as sub-nanometer to tens of nanometer, SWCNT network can be considered as a quasi two dimensional (2D) system [83]. The interconnectivity of such network can be described by using a well-established 2D percolation theory as the following

$$N_c = 4.236^2 \pi {L_s}^2 \approx \frac{1}{L} \tag{3.1.1}$$

where, N_c is the threshold of network, L_s and L are the length and aspect ratio of individual

SWCNTs, respectively. As the aspect ratio is very high, SWCNT has a 1-3 nm of diameter and several micrometers in length, this refers that the threshold of a SWCNT network is very low. Therefore, the amount of materials is not enough as required to make an interconnected path for carrier transport, leading to the high light transmittance. The thin films of SWCNTs with high conductivity as well as transparency are highly desirable for applications as transparent conducting films in flexible electronics.

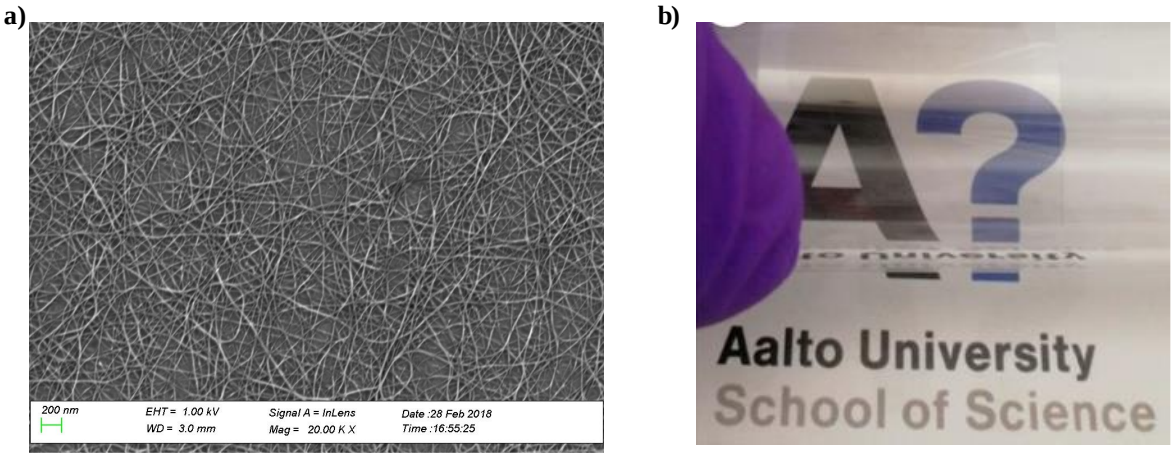

Figure 3.1.1. (a) A typical scanning electron microscopy (SEM) image of SWCNT thin film, (b) Optical photo of SWCNT film on PET. Adapted from [84].

From the formula 3.1, it is evident that the sheet resistance of SWCNT-TCF decreases with the thin film thickness increasing. According to the literature, with the various fabrication methods such as wet or dry process, the conductivity of TCFs changes extensively because of the various geometric and chiral structure of SWCNTs.

To understand the carrier transport within the network researchers have employed a simple model where the carrier transport is along a SWCNT and then jumps to another SWCNT through their junction, though the resistance of SWCNT-TCFs is very complicated. It has been demonstrated that the resistance of SWCNT-TCFs largely assigns to the tube-tube junction resistance, while the resistance with the individual tube contributes slightly. The junction resistance relies on the SWCNT bundle length and diameter as well as the electronic types of SWCNT such as metallic or semiconducting [85,86].

Based upon the similar transmittance, the longer bundles will make fewer junctions compared with the shorter ones, arising to improved conductivity. Simien *et al.* [87] and Hecht *et al.* [88] have studied how the conductivity of CNT thin films depends on bundle length. Moreover, Hecht *et al.* reported that the film conductivity (σ) is directly proportional to the average bundle length (L_{av}) as, $\sigma \propto L_{av}$. However, by studying CNTs with length of 0.4 cm, Li *et al.* proposed that the resistance along the tube is dominated rather than the resistance of the junction [89]. Apart from the the bundle length, the bundle diameter also plays prime role in film conductivity. The charge transport mainly occurs on the surface of bundles, while the whole bundle tubes could be given the light absorption [90]. Therefore, small bundles of SWCNTs are required for highly conductive films. Mustonen *et al.* [56] comprehensively studied the effect of bundle diameter and achieved highly individual SWCNTs by FC-CVD system. After HNO_3 doping, the corresponding TCF illustrates sheet resistance of 63 Ω/sq at 90% transmittance. Jiang *et al.* [76] has synthesized carbon-welded and non-bundled SWCNT network and obtained a sheet resistance of 25 Ω/sq at 90% transmittance after HNO_3 treatment.

Liao *et al*. [13] reported that the tuning of the bundle length and diameter using CO_2 as promoter in FC-CVD, where the SWCNTs with large tube diameter ~ 1.9 nm and a metallic tube ratio of 46.3% form the bundles with length of ~7.5 μm and small bundle diameter ~7.1 nm. They employed filter-press transfer method to make thin films, the corresponding TCF showed 86.8 Ω/sq at 90% transmittance. Laiho *et al*. [91] systematically studied the scale-up deposition of prepared aerosol SWCNTs on 50 mm wafers or the PET with the help of a large size thermophoretic precipitator (TP). Therefore, corresponding TCFs illustrated a comparable uniformity and conductivity to the filter-press transfer films.

Table 3.1. Performance of SWCNT films from literature [24].

Films	Fabrication	Pristine R_s (Ω/sq.)/T	Dopant	Final R_s (Ω/sq.)/T	Ref.
SWCNT	Disperse commercial HiPco CNTs in superacid chlorosulfonic acid and obtained the film by vacuum filtration.	–	HSO_3Cl	60/90.9%	Hecht *et al.* [92]
SWCNT	FC-CVD using CO as carbon source and $FeCp_2$ as catalyst precursor, with a semi-industrial reactor to prepare the longer (9.4 μm) CNT bundles.	820/90%	HNO_3	110/90%	Kaskela *et al.* [48]
SWCNT	FC-CVD with a spark reactor, which can control size and concentration of pre-made catalysts. The SWCNTs have highly individual (>80%) tubes.	–	HNO_3	60/90%	Mustonen *et al.* [56]
SWCNT	FC-CVD with feedstock of $FeCp_2$ dissolved in ethanol, obtaining SWCNTs with mean bundle length ~27 μm.	320/90%	$AuCl_3$	95/90%	Ding *et al.* [93]
SWCNT	FC-CVD using CO and C_2H_4 as mixture carbon source to get long (17 μm) SWCNT bundle.	291/90%	$AuCl_3$	73/90%	Anoshkin *et al.* [94]
SWCNT	FC-CVD using C_2H_4 and toluene ($FeCp_2$ dissolved), growth with high feeding rate, SWCNTs are long (mean 62 μm) and highly individual welded by graphite carbon.	41/90%	HNO_3	25/90%	Jiang *et al.* [76]
SWCNT	FC-CVD using CO as carbon source, CO_2 as growth promotor to modulate tube diameter and length *etc.*	273/90%	$AuCl_3$	86/90%	Liao *et al*. [13]
SWCNT	FC-CVD using CO as carbon source, CO_2 as growth promotor to modulate SWCNT growth, thin films deposited by large TP on glass or PET.	200/87.8%	HNO_3	60/87.8%	Laiho *et al.* [91]

4. Experiment

4.1. Preparation of CNT thin film and sample description

In this work, all the CNTs are synthesized using the FC-CVD method, where the methane (CH_4) is used as carbon source and ferrocene as the catalyst precursor and sulfur is used as the promoter to tune the growth of CNTs.

As shown in Figure 4.1.1a, a vertical furnace (Entech, Sweden, length, 90 cm) equipped with a precursor feeding system, quartz tube (inner diameter, 22 mm) and, sample collecting nitrocellulose membrane filter (Merck Millipore, France, diameter 45 mm). The furnace temperature was set at 1100 °C is used for high temperature CNT growth. Gas flows into the reactor were controlled using a mass flow controller (MFC, Aalborg, USA). Ferrocene (99.0%, Alfa Aesar) is used as catalyst precursor, CH_4 (99.99%, AGA) as carbon source, S (99.9%, Sigma-Aldrich) as growth promoter. N_2 (99.995%) vaporized from liquid nitrogen and H_2 (99.999%, AGA) as carried gas for CNT synthesis. Specially, N_2 is purified by a moisture absorber filter. To introduce ferrocene vapor into the reactor, nitrogen was passed through the cartridge containing the precursor powder. The gas flow and cartridge temperature were controlled to tune the amount of ferrocene and sulfur into the reactor.

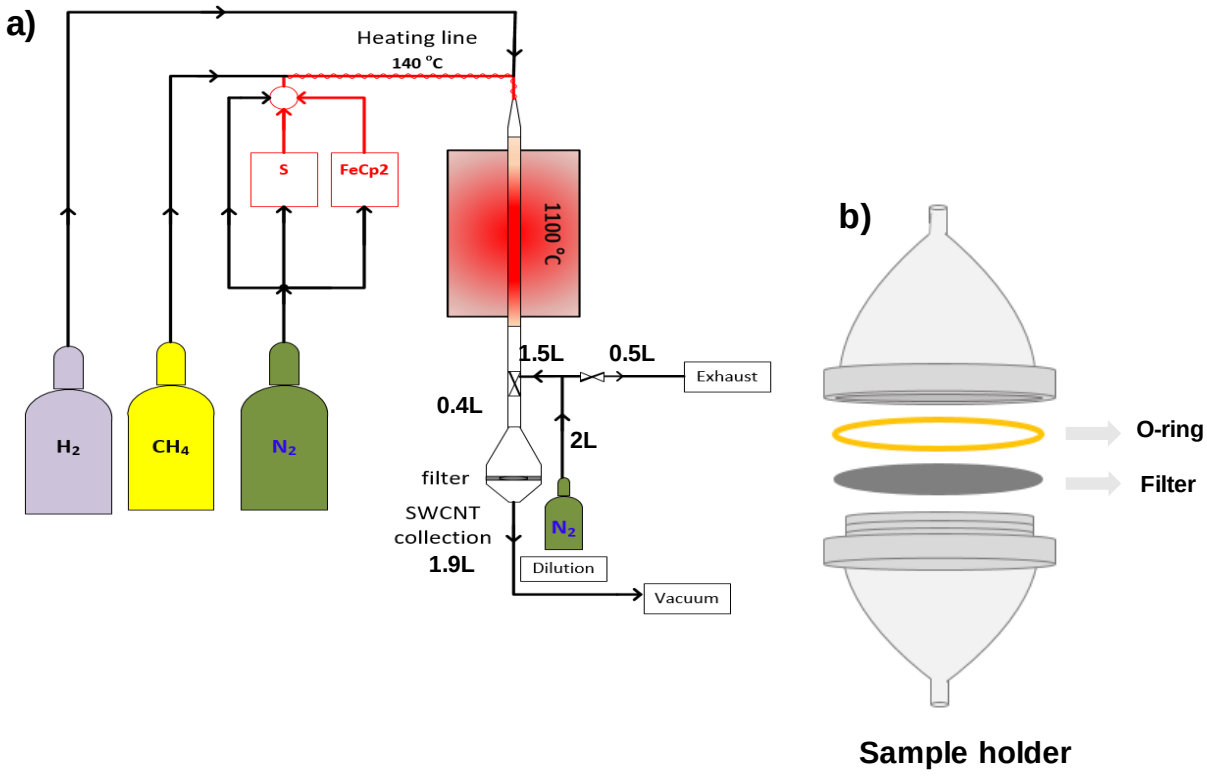

Figure 4.1.1. a) Schematic of the CNT film fabrication reactor where CH_4 is used as a carbon source and ferrocene as catalyst precursor, sulfur is employed as CNT growth promoter. b) The schematic of sample collection holder which is nicely designed for CNTs aerosol deposition onto a membrane filter using vacuum.

The top part of the reactor is connected to the gas inlet and the bottom part is connected to the gas outlet. Ferrocene and sulfur were put in two separated cartridges which can be heated up. A vapor-phase catalyst precursor (ferrocene), a SWNT growth promoter (sulfur) and carbon source (CH_4) were floated into the reactor for CNT synthesis. In addition, H_2 is used to tune CH_4

decomposition. The excess CH_4 decomposition can produce more amorphous carbon, which can inactive the catalysts and degrade the conductivity of the produced SWCNT film. During the process, ferrocene and sulfur were vaporized by heating in cartridge and carried into the reactor with nitrogen as carrier gas.

Total gas flow is around 0.4 slm including N_2, H_2, and CH_4. The flow rate of the carrier gas N_2 for ferrocene and sulfur was 100 sccm and 150 sccm respectively, and then they were mixed with the other 80 sccm N_2, 70 sccm H_2, and 8 sccm CH_4 into the furnace, as depicted in Figure 4.1.1a. Since the saturated vapor pressure of ferrocene and sulfur increase with temperature, higher heating temperature means that higher concentration (pressure) of ferrocene and sulfur are introduced to the furnace tube. The temperature of the furnace was set at 1100 ℃ and the vacuum flow was controlled by the MFC system. During the whole experiment, the amount of CH_4, N_2, and S were tuned, by adjusting the flow rate and temperature respectively. The furnace temperature set for the reaction was maintained at 1100 ℃ based on previous trials, and typical collection time for each film was between 1 min and 30 min as shown in figure 4.1.1a. Correspondingly, the CNTs will grow in a laminar flow and thin films will be collected in the outlet of the reactor. The aerosol CNT samples are collected using two different technics, the filter-press transfer [95] and the thermophoretic precipitator (TP) [96].

As shown in Figure 4.1.1b, a filter with 0.45 μm pore size is placed in a cone-shaped holder, one top of the filter an O-ring is used for sealing. Then the aerosol CNTs are collected on the filter with the help of a vacuum, the CNT film thickness can be controlled by varying the collection time. Lastly, the CNT films on the filter can be directly transferred on various substrates by pressing.

4.2. Doping of CNTs

To further improve the conductivity of CNT thin film, doping is generally employed. Doping improves CNT conductivity in two ways: the carrier concentration in the networks can be increased, the tube-tube junction resistance can be reduced. In this thesis, we used Gold (III) ($AuCl_3$: purity 99%, Sigma-Aldrich) as a dopant for two reasons. Firstly, sheet resistances of $AuCl_3$ doped CNT films are relatively stable at ambient conditions. Secondly, the intrinsic structure of CNTs could be preserved after $AuCl_3$ treatment. The CNT films on membrane filters were press transfer to quartz slides (35 × 20 × 1mm, Finnish special glass). The $AuCl_3$ powder was dissolved in acetonitrile (99.8%, Sigma-Aldrich) to a concentration of 16 mmol/L as the doping solution to the TCFs. Since the solution is very sensitive to light, it was wrapped by foil to avoid decomposition. As shown in Figure 4.2.1, after measuring pristine CNT film, the sample is placed in the fume hood, then some drops of $AuCl_3$ in acetonitrile solution (16 mM) were placed on to the CNT film until the whole film was immersed in the solution. After a residual time of 5 min, the solvent was washed away by pure acetonitrile and then the film was dried with N_2 by air low gun. The sheet resistance will be measured again right after doping.

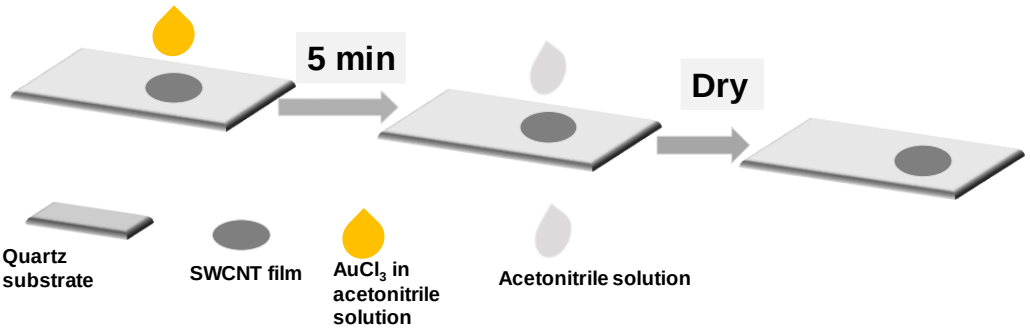

Figure 4.2.1. Schematic representation of the doping process of CNT thin film by $AuCl_3$.

4.3. Characterization

4.3.1. Optical Spectroscopy

The optical absorption spectroscopy (OAS) technique is used to study the diameter, metallic or semiconductive tube ratio, and doping level of CNT TCFs. In this thesis, we employed this method to insight the diameter of CNTs. To measure the absorption spectra of the CNT thin films, the sample was transferred via a dry transfer technique from the filter to an optically transparent substrate, comprised of a 1 mm thickness quartz window (material: HQS300, Heraeus).

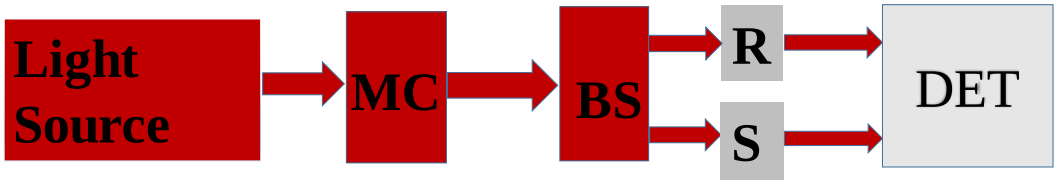

Figure 4.3.1. The schematic representation of the typical UV-vis-NIR spectrometer where deuterium lamp is used as a light source, through the monochromator (MC), beam splitter (BS), reference (R) and sample (S), and to the detector (DE).

The optical transmittance T (at 550 nm) and the UV-vis optical absorption were performed using a dual-beam spectrophotometer (UV- Vis-NIR Agilent Cary 5000). It is equipped with two excitation sources (a deuterium lamp and a halogen lamp), which together covers the working wavelength range from 175 to 3300 nm. The electromagnetic wave with all wavelengths is produced by a light source, then passed through a monochromator. Monochromator is used to

get a single wavelength of light. Then beam splitter is employed to split a single beam of light into two rays where one ray passing through a sample and other one through reference. After the calibration, an uncoated substrate was used with a reference beam to exclude the effect of the substrate. The light then goes towards the reference and the sample when recorded by a detector. The detector compares the reference value I_0, to the sample value, I. Thus, the absorption spectrum can be produced.

To understand the macroscopic properties of CNT films, we used optical absorption spectroscopy and to investigate the CH_4 effect UV–vis–NIR spectroscopy is an efficient and comprehensive method to analyze the diameter distribution, all tubes will contribute to the absorption spectra [93].

Raman spectroscopy technique is used to investigate the quality and diameter of CNT TCFs in this work. In case of Raman spectroscopy, the CNTs are transferred on quartz slide similar to OAS measurement. In this work, Raman spectra were obtained using a Raman spectrometer (Horiba Jobin-Yvon Labram HR 800) equipped with three distinct excitation wavelengths 488 nm, 514 nm, and 633 nm.

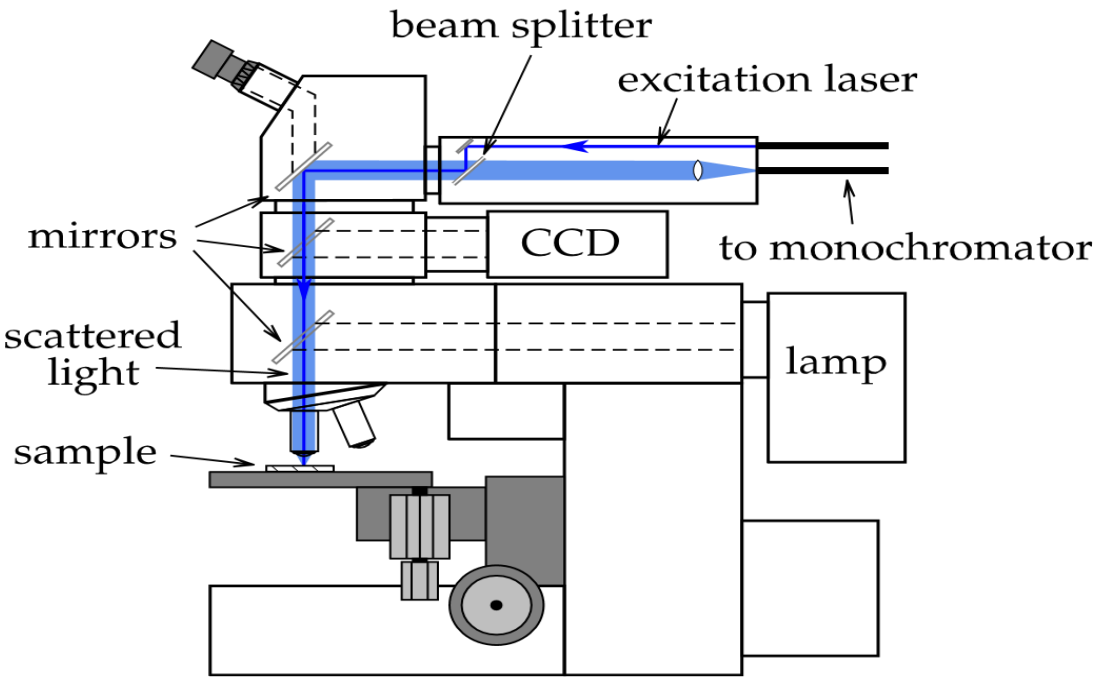

Figure 4.3.2. Illustration of the resonant Raman spectrometer including different excitation sources [29].

In Raman spectroscopy, equipment is used to measure the Raman spectra which consists of an excitation laser, and it is well designed for increasing the Raman scattering event frequency to obtain a decent measurement of the scattered light signal. To enhance this signal, the laser was placed to focused on a small area of the sample while the signal was measured. The microscope optical lenses are used to focus the laser beam and these lenses can also be used to collect the scattered light, which is sent into a charge coupled device (CCD) to record through a monochromator. A dichroic mirror (beam splitter) and an adjustable edge filter were used to reduce the intensity of the Rayleigh-scattered light before it passes through the monochromator [97].

4.3.2. Scanning Electron Microscopy

Scanning electron microscopy (SEM) is widely used to investigate the morphology such as tube (bundle) lengths, density, defect, or impurities of SWCNTs. In this thesis, we used SEM to study the nanotube lengths.

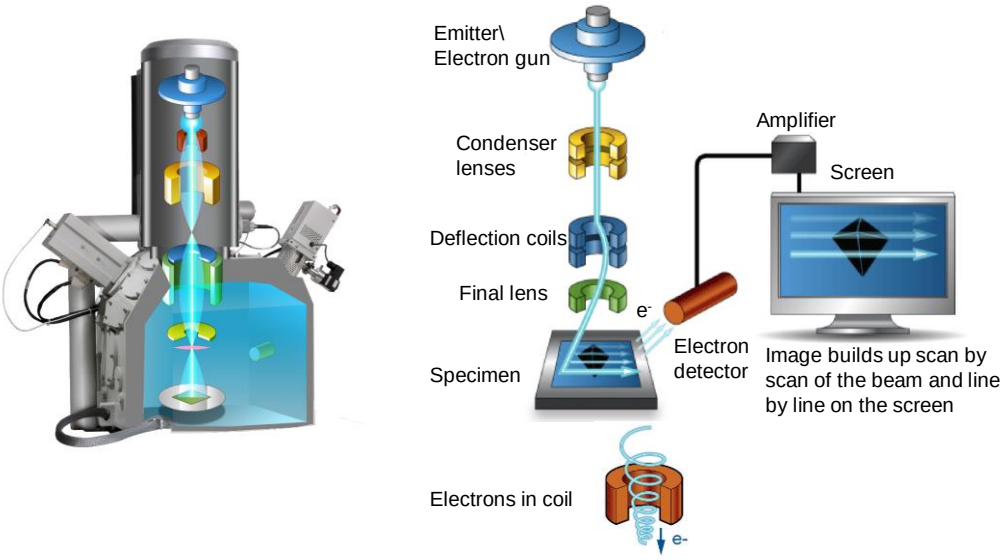

Figure 4.3.3. The schematic diagram of scanning electron microscope (SEM). Image adapted from [98].

To create a magnified image of a sample, the SEM uses a focused beam of high energy electrons. The electron is emitted from an electron gun. With the assistance of acceleration voltage, the electrons are passed through the condenser lens and the objective lens. Thus, an electron beam is formed with a few nanometers diameter. The electron signals are generated by using the beam-specimen surface processes if the electron beam bombards the surface of the specimen. When the electron beam is scanned across the specimen surface, the electron signals are detected by the detector. Therefore, these signals are shifted into the corresponding points based on the number of detected electrons and displayed on a screen. Thus, the SEM image is formed as a serial data stream which is called electron image [99].

As CNTs are very small and were deposited on an insulating substrate, such as Si/SiO_2 or quartz, the samples have to be observed by an in-column-type (in-lens) secondary electron detector at 1.0 kV acceleration voltage. In order to study the CNT bundle length by SEM, the aerosol CNTs were deposited on Si/SiO_2 substrate by filter press transfer method. Then the bundle length distribution was analyzed using software ImageJ by counting all the CNTs shown in SEM image.

4.3.3. Transmission electron microscopy

Transmission electron microscopy (TEM) is a powerful method to analyze the nanoscale structure of SWCNT. In our work, we employed a JEOL 2200FS Double Cs-corrected TEM for high-resolution imaging at 200 kV. To prepare a TEM sample, we placed the TEM grid on the membrane filter, followed by putting them in the holder and harvesting SWCNTs with the assistance of a vacuum.

4.3.4. Sheet Resistance Measurement

The sheet resistance (Rs) method is used to analyze the electrical properties of a thin film, such as metal or doped semiconducting thin films. The Rs of SWCNT TCFS was measured by a Jandel test unit (model, RM3000) equipped with a 4-point probe head (Jandel, UK), consisting of four in-line tungsten tips with a 300 μm curvature, loading force of 15 g each (60 g total) and 1.0 mm separation. For the sheet resistance measurement, the SWCNT thin films were transferred on the quartz substrate by filter-press method, then the 4-point probe system was applied. When the thickness t is small compared to the probe distance s, the sheet resistance can be calculated by the following formula Rs = $\frac{\pi}{ln2}\frac{U}{I} = 4.53\frac{U}{I}$, where U is voltage and I is the current [100].

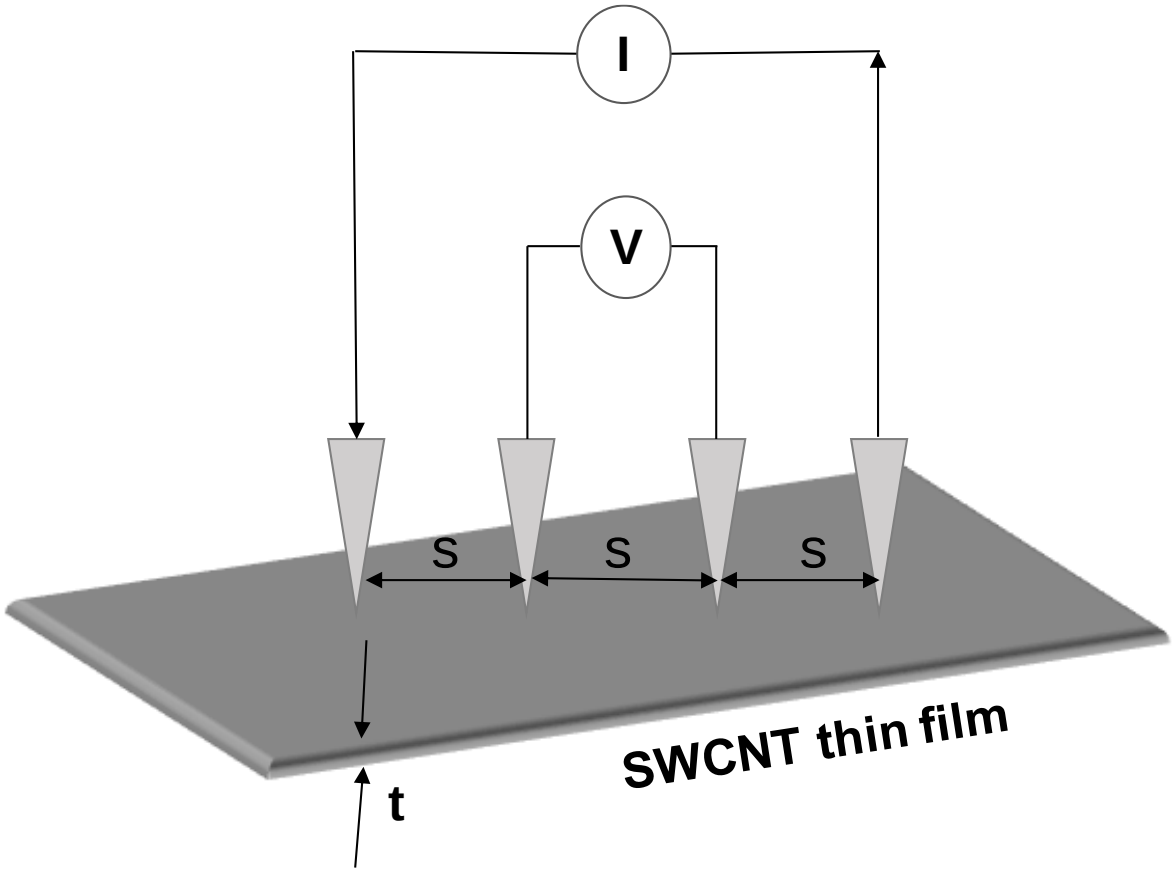

Figure 4.3.4. A schematic illustration of 4-probe setup where t is the thickness of the film and probe distance is referred to s. A constant current is supplied from outer probes and the voltage drop is recorded by the middle probes.

5. Results and Discussion

5.1. Effect of collection gas flow on the uniformity of the film

In this study, we first investigate the effect of collection gas flow. As the conventional collection method, firstly the films were collected with the 0.4 slm gas flow. Therefore, the collected films are not homogeneous and these specific patterns on the film caused by the laminar flow due to the low gas flow. In a further study, we increased the collection gas flow to make turbulence gas flow for the homogenous CNT film. When we increased collection gas flow over 1.8 slm (0.4 slm from CNT synthesis and 1.4 slm from side N_2 gas flow), we obtained a uniform CNT film. Based on this investigation we used 1.8 slm collection gas flow for further experiments.

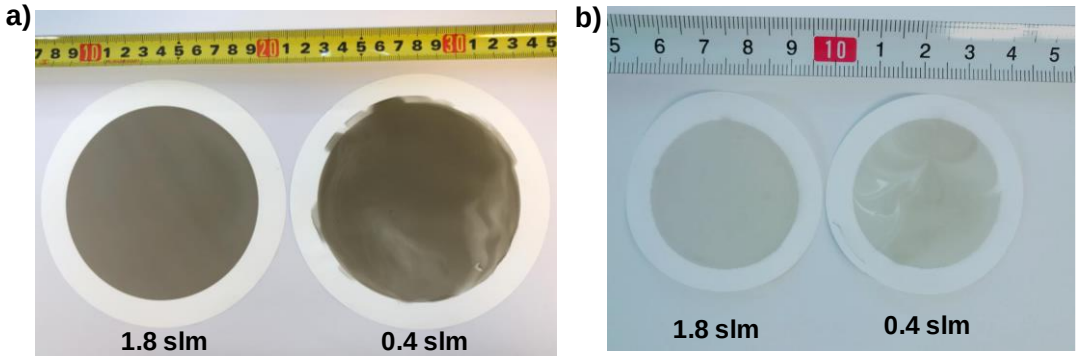

Figure 5.1.1. Optical images of CNT film on the filter with diameter of a) 10 cm, b) 4.7 cm diameter filter with 1.8 slm and 0.4 slm collection gas flow.

5.2. Optimization of the recipe for high yield CNT synthesis

Here, the $FeCp_2$ cartridge was set at 45 °C and N_2 gas flow with 100 sccm for the high yield CNT growth. The saturated vapor pressure of $FeCp_2$ at 45 °C is around 6 times higher than that at 25 °C. The reactor was set at 1100 °C and total gas flow fixed at 400 sccm for the constant synthesis time. Then, the CH_4, H_2, and S were optimized based on the CNT film yield and performance.

5.2.1. CH_4 effect on CNT synthesis

As shown in Figure 5.2.1, the CH_4 from 5 to 11 sccm was optimized with 50 sccm H_2 and 150 sccm N_2 through sulfur cartridge at 105 °C (Fe:S = 4:1). Compared to SWCNT films from other FCCVD systems (e.g. CO [13], C_2H_4 [14] or C_2H_6O [15]), the CNT films from this CH_4 system have weak and broad absorption peaks in the visible and infrared regions. As illustrated in Figure 5.2.1a, the typical optical absorption spectra of CNT films was synthesized with various CH_4 concentrations. From the absorption peak location, the nanotube from the lower CH_4 concentration gives the smaller CNT diameter. The mean diameter can be estimated based on the position of the absorption peaks. In this study, the S_{11} peak lies at 1572 nm. Based on the Kataura plot, the mean diameter of CNT estimated is around 1.2 nm.

According to Figure 5.2.1b, CNT yield changes with the variation of CH_4 concentration. The yield is normalized with respect to yield for 8 sccm CH_4 concentration. With the increase of CH_4 concentration, the CNT yield is also increased. Here, the CNT films with 4.7 cm diameter have around 90% transmittance with 4 min collection. For example, the yield for 5 sccm CH_4 is around 30% compared that for 8 sccm CH_4, but the yield at 11 sccm CH_4 is two times higher than that 8

sccm CH_4. It shows that the addition of higher carbon source in the system, produces more CNTs which in turn synthesizes higher yield.

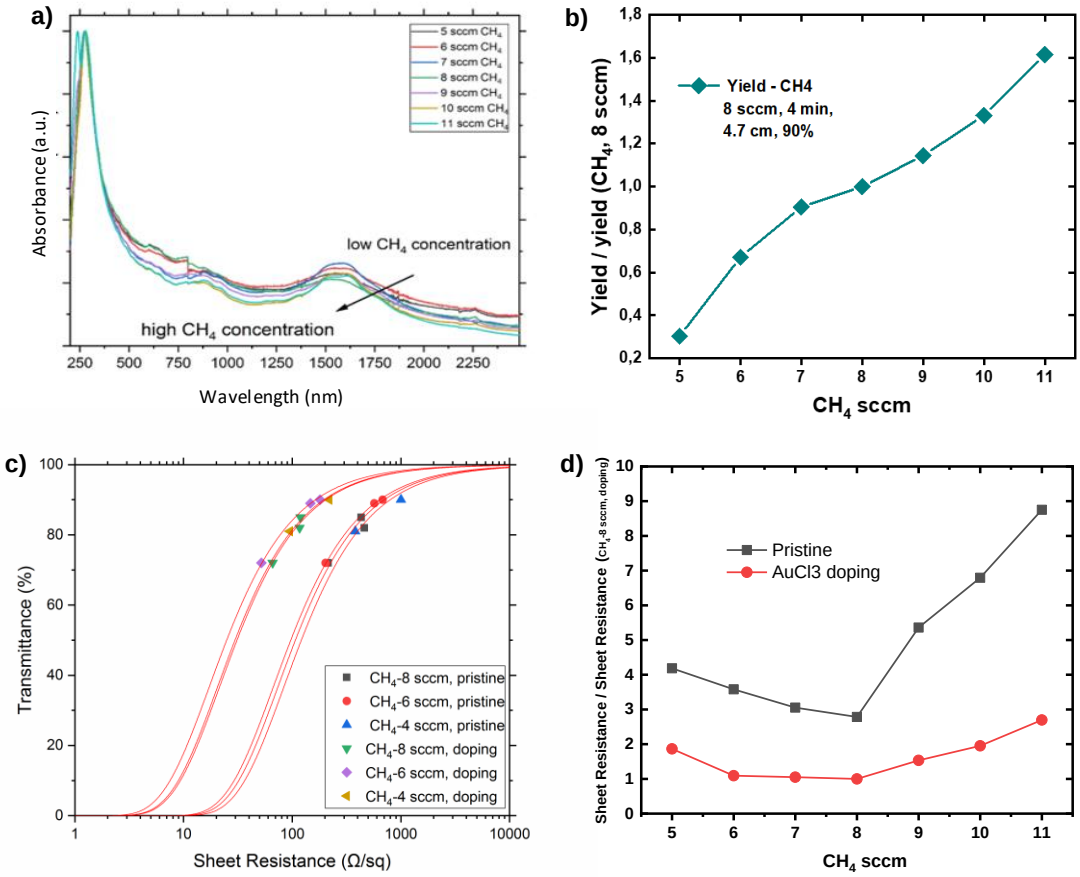

Figure 5.2.1. The optical absorption spectra, yield, optoelectronic performance of CNT films, and conductivity with various CH_4 amount. a) UV-vis-NIR optical absorption spectra for the set of CNT films with different CH_4 concentrations. b) Yield effected by different CH_4 concentrations c) Optoelectronic performance of CNT TCFs evaluated by sheet resistance vs. transmittance. The sheet resistance (Ω/sq) vs. transmittance (%) at 550 nm wavelength of pristine and $AuCl_3$ doped CNTs based transparent conductive films using CH_4 as a carbon source. d) Sheet resistance based on various CH_4 amounts before and after $AuCl_3$ doping.

To further get insight on the effect of carbon source CH_4 on CNT TCFs, we fabricated films with various transparencies by collecting samples with different collection times. The films were directly transferred on transparent quartz slides by a press-transfer technique [48] for measuring transmittance. A plot of data points having different transmittance versus sheet resistance is shown in Figure 5.2.1c. Data points were fitted by following the formula 3.1, where K is constant of proportionality which depends on the optical and electronic properties of CNT based TCFs. For the pristine CNT films, the sheet resistance value of the 90% transmittance (@ 550 nm) CH_4 of 8 sccm CNT film (627 Ω/sq) is much lower than those with CH_4 of 6 sccm (702 Ω/sq) and CH_4 of 4 sccm (802 Ω/sq) CNT films.

To further improve the conductivity, we doped CNTs film with $AuCl_3$ which is considered to be a more stable dopant for CNTs [101]. Doping of CNTs with $AuCl_3$ shifts the Fermi level of both metallic and semiconducting nanotubes down towards the valance band [102] which helps to improve the conductivity of the film. After $AuCl_3$ treatment, the sheet resistance of films at 90% transmittance decreases to 196 Ω/sq for 6 sccm CH_4, 165 Ω/sq for 8 sccm CH_4 and, 205

Ω/sq for 4 sccm CH_4. The sheet resistance value of 165 Ω/sq for 90% transmissions from 8 sccm CH_4 is one of the best reported values among them.

However, the change of CNT film conductivity is not monotonic. The film conductivity first increases and then decreases with CH_4 concentration increase, as shown in figure 5.2.1d. As noticed for pristine films, with the CH_4 concentration increase, sheet resistance decreases till 8 sccm CH_4, so the highest conductivity is obtained for 8 sccm CH_4. Then sheet resistance is increasing at higher concentration of CH_4 because higher concentration of CH_4 gives more amorphous carbon which decreases the performance of the film. After $AuCl_3$ treatment, the sheet resistance is also decreasing till 8 sccm CH_4 so the film conductivity improved and then the film conductivity decreased with CH_4 amount increase Figure 5.2.1d. In summary, the best performance CNT films are from 8 sccm CH_4, which has a sheet resistance value of 165 Ω/sq for 90% transmission.

5.2.2. Effects of H_2 on CNT growth

Here, the CH_4 concentration was fixed at 8 sccm and we optimized the H_2 concentration from 40 to 80 sccm. To study the macroscopic properties of CNT films we firstly used UV-vis-NIR optical absorption spectroscopy to investigate the H_2 effect. The typical absorption spectra of CNT film with varying H_2 is shown in Figure 5.2.2a. The CNT diameter is not sensitive with H_2 increase. The CNT yield is normalized based on the H_2 concentration at 70 sccm. Importantly, the yield is found to decrease with increasing the H_2 concentration (Figure 5.2.2b). For pristine films, with the H_2 concentration increase, the sheet resistance decreases till 70 sccm H_2 and then sheet resistance increases at a higher concentration of H_2 (Figure 5.2.2c). In short, the yield is decreasing with increasing the amount of H_2. The conductivity of nanotube films first increases and then decreases. We reported the best performance CNT film from 70 sccm H_2.

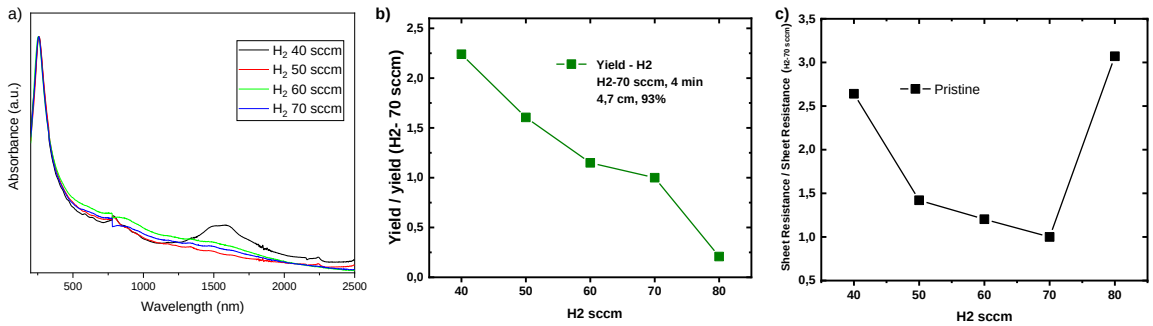

Figure 5.2.2. The optical absorption spectrum, yield, and conductivity of CNT film with various H_2 amount. a) The optical absorption spectra of CNT film with various H_2 b) Yield changes based on the concentration of H_2. c) Sheet resistance at varying H_2 for the pristine film.

5.2.3. Sulfur dependence

Herein, we keep CH_4 of 8 sccm and 100 sccm N_2 through the $FeCp_2$ cartridge at 45 ^oC, and H_2 of 70 sccm are fixed. Then we optimized the N_2 through S cartridge at 105 ^oC from 50 to 250 sccm (for the condition of 50 sccm N_2 through S cartridge with 105 ^oC, write as 50 sccm S). Optical absorption spectra were first studied. A typical absorption spectrum of CNT films with various sulfur is shown in Figure 5.2.3a. Absorption peak from 1200 nm to 2000 nm is related to the CNT diameter. The higher sulfur concentration produces the smaller CNT diameter.

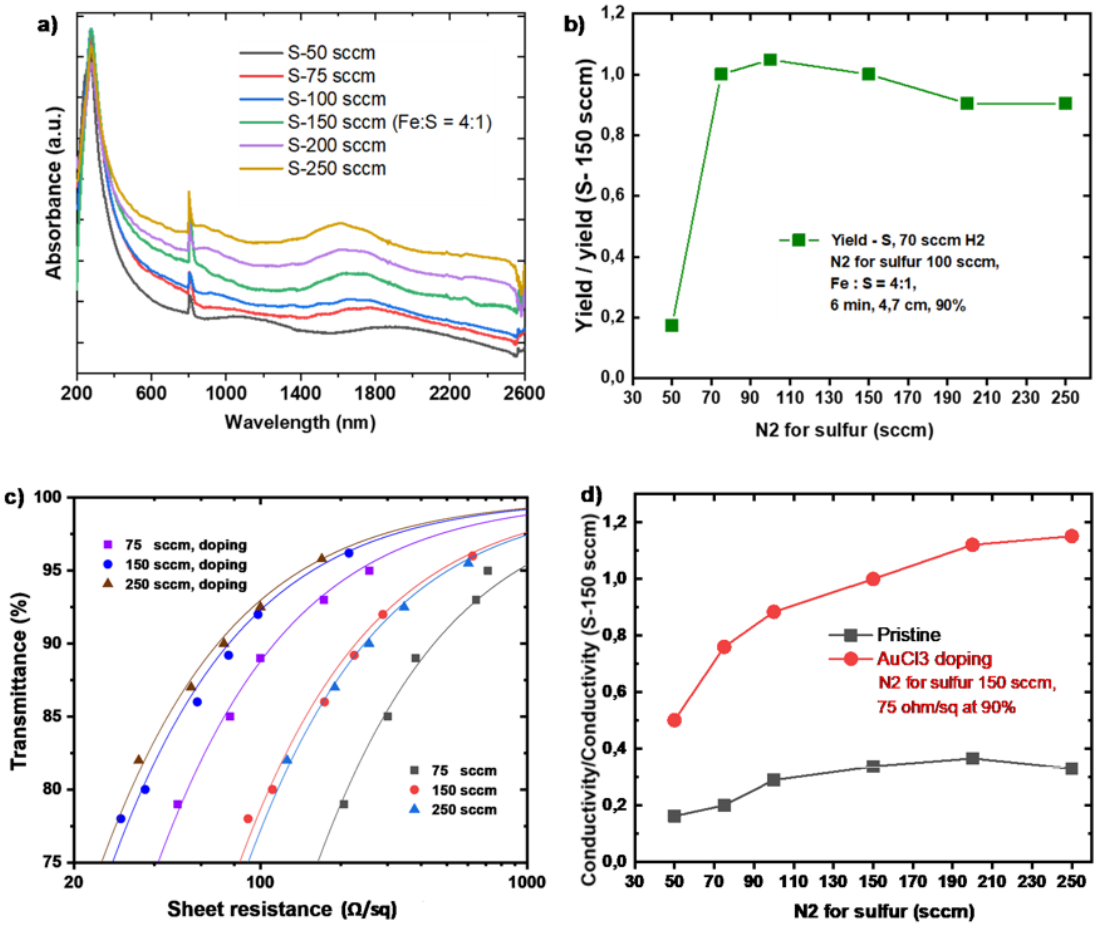

Figure 5.2.3. The optical absorption spectra, yield, the optical performance of the CNT films, and conductivity of CNT films with various sulfur concentration. a) Optical absorption spectra of CNT films with varying sulfur. b) Variation in normalized yield with the change in amount of sulfur from 50 sccm to 250 sccm. c) The sheet resistance versus optical transparency for pristine films and $AuCl_3$ doped films. d) Corresponding variation in specific conductivity of pristine and doped films.

The CNT yield is normalized based on the 150 sccm sulfur. With the sulfur concentration increases, the CNT yield increases rapidly till 70 sccm Sulfur. Then the yield slightly decreases (Figure 5.2.3b). Notably, the CNT film performance is similar from 150 to 250 sccm sulfur, but the yield decreases. It can be seen from Figure 5.2.3c, the optical performance of the CNT films for before and after doping with $AuCl_3$, the sheet resistance at 90% $T_{550\ nm}$ for CNT films with different sulfur concentrations. As noticed for pristine films, the sheet resistance decreases with the increase of sulfur concentration. The sheet resistance of a pristine film with 90% transmittance with 75 sccm S is 400 Ω/sq, 150 sccm S is 180 Ω/sq, and 250 sccm S is 150 Ω/sq respectively. After doping, the sheet resistance of a doped film with 90% transmittance becomes 100 Ω/sq, 75 Ω/sq, 80 Ω/sq by using 75 sccm S, 150 sccm S and 250 sccm sulfur respectively. The Conductivity of nanotube films increases with sulfur concentration increase (Figure 5.2.2d). In summary, the CNT yield increases with the S amount increase. The best performance CNT films are from 150 sccm S, which has a sheet resistance value of 75 Ω/sq for 90% transmission. The conductivity of CNT film is improved with S increasing.

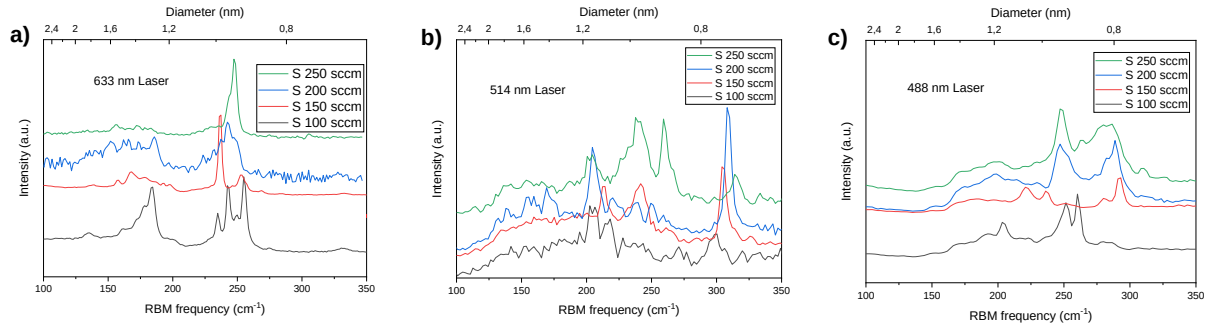

Figure 5.2.4. RBM of CNTs synthesized with various sulfur concentrations. Laser wavelengths: a) 633 nm, b) 514 nm and c) 488 nm, respectively.

Raman spectra were used to estimate the diameter of CNTs. As shown in Figure 5.2.4 (a-c), the Raman spectra in the range of 100-350 cm^{-1} illustrate the characteristic radial breathing mode (RBM) of CNTs. According to the following relationship, $\omega_{RBM} = A/d_t + B$, where A = 217.8 and B = 15.7 for CNT thin film samples, the diameters of CNTs can be calculated from the frequencies of RBM peaks. For example, with the excitation wavelength of 633 nm laser, RBM peaks of CNT moved from higher frequencies to lower frequencies with the decreasing sulfur from 250 to 100 sccm, which reflects the diameter of tubes becoming larger. The same trends are found with laser wavelength of 514 and 488 nm.

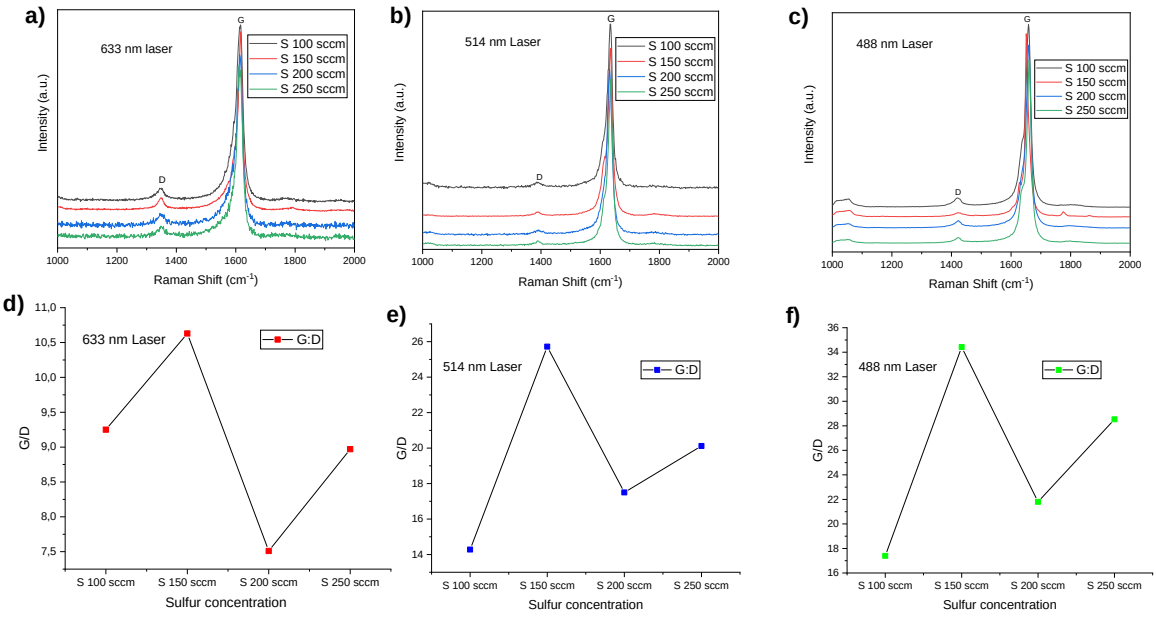

Figure 5.2.5. G and D bands of CNTs synthesized with different sulfur concentrations. Laser wavelength: a) 633 nm, b) 514 nm and c) 488 nm, and the corresponding height ratio of G and D bands, I_G/I_D in d), e) and f), respectively.

To estimate the quality of CNT films, Raman spectroscopy method has been used. The intensity ratio of graphitic (G) band (approx. 1590 cm^{-1}) to disorder (D) band (approx.1340 cm^{-1}), I_G/I_D, in Raman spectrum is usually evaluate the quality of CNT films. All the I_G/I_D values of the Raman spectra are illustrated in (Figure 5.2.5d-f). With the excitation of 633 nm laser, the I_G/I_D value of CNTs prepared by 150 sccm sulfur is the highest, suggesting the best quality of CNTs. The similar trends are found with the other two excitation wavelengths of 514 and 488 nm laser. It does mean that the quality of CNTs has been improved with 150 sccm sulfur.

5.3. Relationship between yield and performance

Our other (CO [13], C_2H_4 [14] or C_2H_6O [15]) FCCVD systems reported that the low yield can give a better performance from straight nanotubes with small bundle diameters. CNTs in the gas phase by FCCVD follows Brownian motion so low yield can reduce the collision of CNTs in the gas phase, reducing the bundle diameters. The small bundle diameter and long CNT will benefit film conductivity.

Here, we tune the CNT yield and study the effect on the film performance. We change the temperature of $FeCp_2$ and sulfur cartridges, but keep CH_4 of 8 sccm, H_2 of 70 sccm and Fe : S ratio of 4, based on the optimized condition. The optical absorption spectra of CNT films synthesized with different ferrocene and sulfur concentrations are shown in Figure 5.3.1a, Optical absorption technique is used to analyze the macro properties of CNT films. There is no dramatic change with those three absorption peaks. Afterward, we have manufactured CNT films with different transparencies by varying the collection time and plotted against sheet resistances, as shown in Figure 5.3.1b. Accordingly, the normalized yield could be calculated. It can be seen that the yield is decreasing with the $FeCp_2$ temperature decrease (Figure 5.3.1c). Moreover, the CNT TCFs from various $FeCp_2$ and S temperatures illustrate different levels of conductivity. For pristine and doped films, the sheet resistance is found to first decrease and then increase with yield decrease. For example, the sheet resistance of pristine CNT films at 90% $T_{550\,nm}$ decreases from 226 Ω/sq ($FeCp_2$ 45 °C, S 105 °C) to 202 Ω/sq ($FeCp_2$ 40 °C, S 100 °C), but increase to 298 Ω/sq ($FeCp_2$ 35 °C, S 95 °C) and to 686 Ω/sq ($FeCp_2$ 30 °C, S 88 °C). For improving the conductivity of CNT TCFs, $AuCl_3$ solution was used as an efficient dopant. A similar trend was also found in doped films (Figure 5.3.1d). The sheet resistance of doped TCFs firstly reduces from 79 Ω/sq to 59 Ω/sq, then increases to 65 Ω /sq and to 183 Ω/sq at 90% transmittance with yield decrease. Importantly, the lowest obtained sheet resistance of a doped CNT film with 90% transmittance is 59 Ω/sq, ($FeCp_2$ 40 °C, S 100 °C), which is the best sample among them.

CNT yield increases with ferrocene temperature increase. But, the performance of CNT film first increased and then decreased, which conflicts with our previous conclusions of better performance from lower SWCNT yield. Here, the CNT films exhibiting the best performance are from $FeCp_2$ 40 °C, with the sheet resistance value of 59 Ω/sq by $AuCl_3$ doping at 90% transmission on 4.7 cm diameter filter with 10 min collection. It is worth mentioning that the yield of CH_4-based CNT film at 40 °C of $FeCp_2$ is much higher than those of other SWCNT films, e.g. 20 times of CO-based SWCNT films with 86.8 Ω/sq at 90 T% [13], 150 times of C_2H_4-based SWCNT films with 51 Ω/sq at 90 T% [14] and 10 times of C_2H_6O-based SWCNT films with 78 Ω/sq at 90 T% [15].

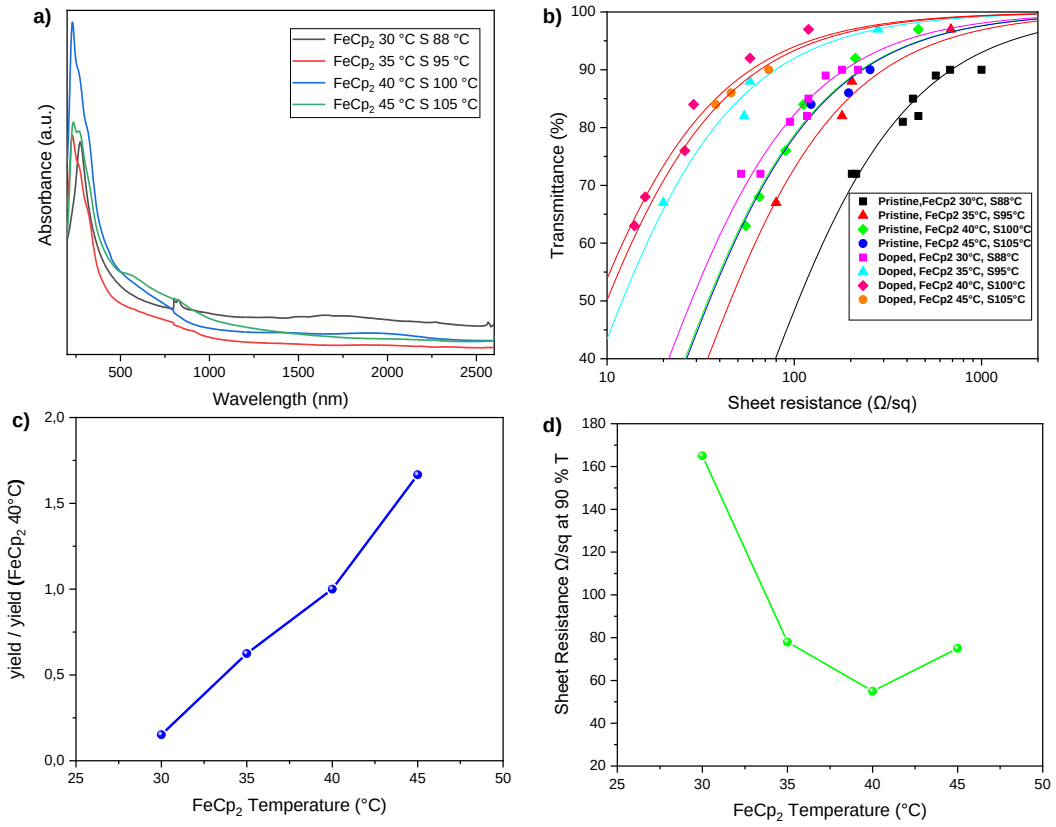

Figure 5.3.1. Effects of $FeCp_2$ and S temperature a) UV–vis–NIR absorbance spectra of CNT film with different Ferrocene and Sulfur concentrations. b) Optoelectronic performance of CNT TCFs by sheet resistance versus transmittance at 550 nm for undoped films and doped films with $AuCl_3$. c) The yield of CNT film with the effect of $FeCp_2$ temperature, and d) The relationship between $FeCp_2$ temperatures versus sheet resistance at 90% transmittance, the CNT TCF with 40 °C temperature displays a sheet resistance of 59 Ω/sq at 90% $T_{550\,nm}$ after doping, which is the lowest among all the samples.

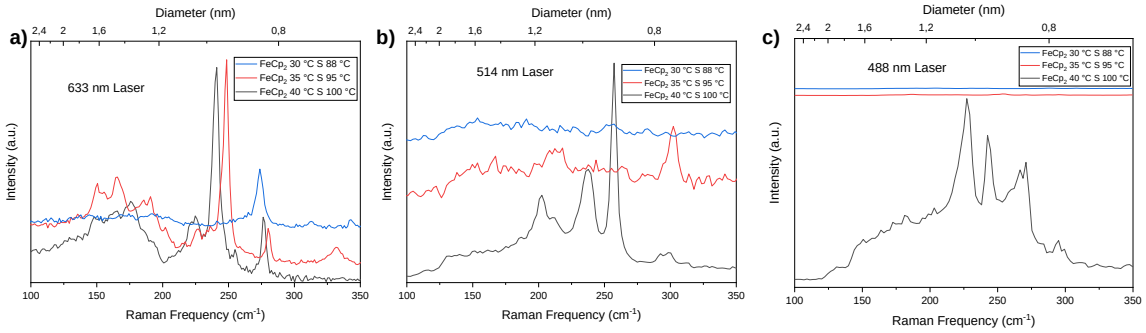

Figure 5.3.2. RBM of CNTs synthesized with various ferrocene and sulfur concentrations. Laser wavelengths: (a) 633 nm, (b) 514 nm and (c) 488 nm, respectively.

Figure 5.3.2a-c, shows the radial breathing mode (RBM) in Raman spectra of CNT thin films. The diameters of CNTs can be calculated from the RBM frequency with the relationship $\omega_{RBM} = A/d_t + B$, where A = 217.8 and B = 15.7. The diameters of tubes increase when $FeCp_2$ and S temperature increases (laser wavelength of 633 nm, Figure 5.3.2a). The same trends are found with the laser wavelength of 514 nm (Figure 5.3.2b). However, the different trends are found under the excitation wavelength of 488 nm, the RBM peaks are disappeared with $FeCp_2$ 30°C, S 88 °C; $FeCp_2$ 35 °C, S 95 °C; they are only visible when the $FeCp_2$ 40 °C and S 100 °C (Figure 5.5.2c).

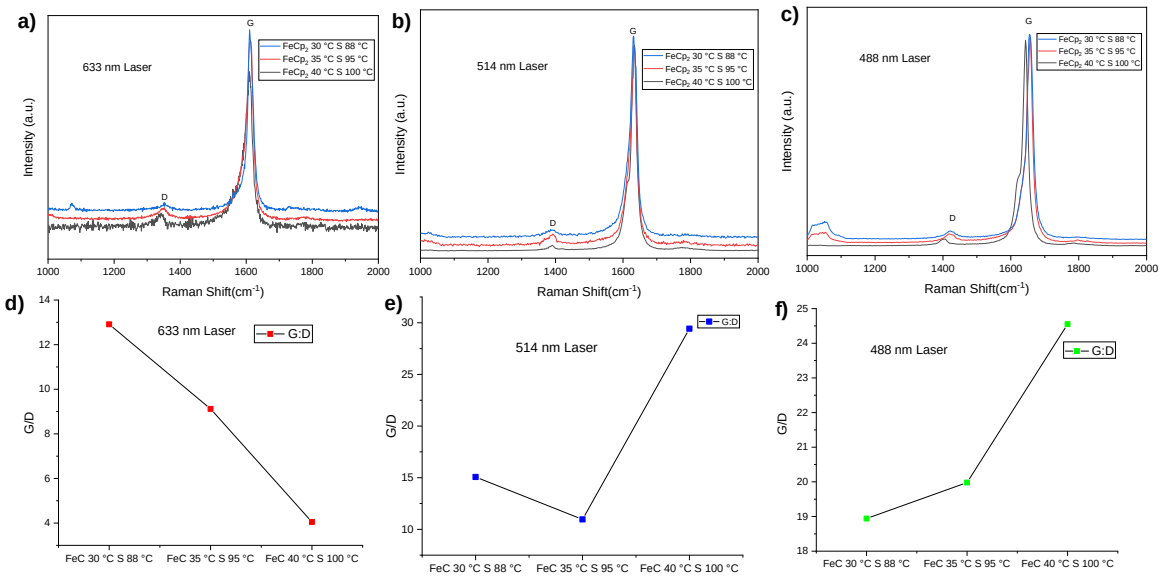

Figure 5.3.3. G and D bands of CNTs synthesized with different ferrocene and sulfur concentrations. Laser wavelengths: (a) 633 nm, (b) 514 nm and (c) 488 nm, and the corresponding I_G/I_D in (d), (e) and (f), respectively.

As shown in Figure 5.5.3, Raman spectra at the excitation wavelength of 633, 514 and, 488 nm were used to study the quality of CNTs. The intensity ratio of G (cm^{-1}) and D (cm^{-1}) band (I_G/I_D) exhibits the quality of CNTs. The higher the ratio, the higher the purity and fewer defects. The height ratio of G and D band, I_G/I_D values are shown in (Figure 5.5.3d-f). With the excitation wavelength of 514 and 488 nm, the I_G/I_D values of CNTs have the highest value with the highest ratio of $FeCp_2$ to Sulfur. However, the reverse trends are found with the excitation wavelength of 633 nm, the I_G/I_D values of CNTs has the lowest.

5.4. Morphology of CNT bundle

In this high-yield CNT FCCVD system, we found a distinctive result of the performance-yield relationship that the film conductivity is not monotonically reduced, but first improved and then declined with yield increase. To understand this result, we applied TEM and SEM to analyze the morphology of CNTs produced with $FeCp_2$ temperature of 40 °C.

5.4.1. Bundle diameter

Here, we employed TEM method to investigate the tube and bundle diameter of CNTs. Surprisingly, we found both SWCNTs and DWCNTs simultaneously produced in this high-yield FCCVD system. Wherein, the proportion of DWCNTs (Figure 5.4.1a) with a diameter of 3.5-6 nm is up to 80%. SWCNTs with small diameters prefer to form bundles. The bundle diameter was estimated to be 8.3 nm (Figure 5.4.1b) and 35% of the CNTs are individual. Considering the high proportion of large-diameter DWCNTs, these bundles with a mean diameter of 8.3 nm are still quite ‘small’.

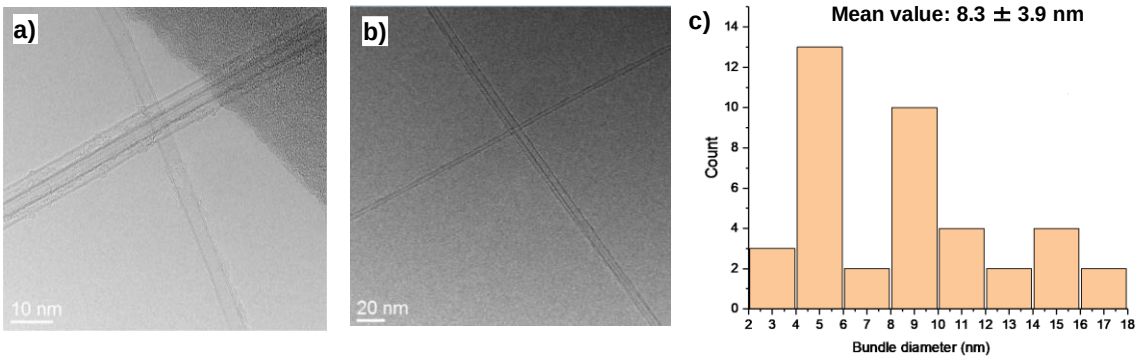

Figure 5.4.1. CNT bundle analysis based on TEM. The typical TEM images (a), (b). c) The distribution of CNT bundle diameter.

5.4.2. Length of CNT bundles

In order to deeply understand the causes of the high performance of CNT films, the microscopic structure of the synthesized CNTs was studied [93]. Sparsely distributed CNTs were collected onto a SiO_2/Si substrate by using a press transfer method for the length measurement of the CNT bundles with the scanning electron microscope (SEM; Zeiss sigma VP) [84]. As shown in Figure 5.4.2a, all the tubes are quite straight with few clusters or loops, being beneficial for electrical conductivity. Contact junction resistance plays a key role in the thin film conductivity. The longer tubes have fewer contact junctions compared to shorter tubes under same transmittance, fewer junctions are beneficial for electrical conductivity. The CNTs with longer bundle length, as we discussed above, show potential for better TCF performance. In 2018, Liao *et al.* [13] introduced a certain amount of CO_2 in FC-CVD reactor where CO was used as a carbon source. They found that the bundle length of SWCNTs increases with CO_2 concentration, and the mean length is of 7.5 μm when introducing 0.50 % CO_2 to a reactor. Here, the CNT bundles are collected in 20 s on a 10 cm diameter filter and then transfer on Si substrate by press. The mean length of CNT bundles is 14.52 μm based on the statistics from 85 bundles (Figure 5.4.2b).

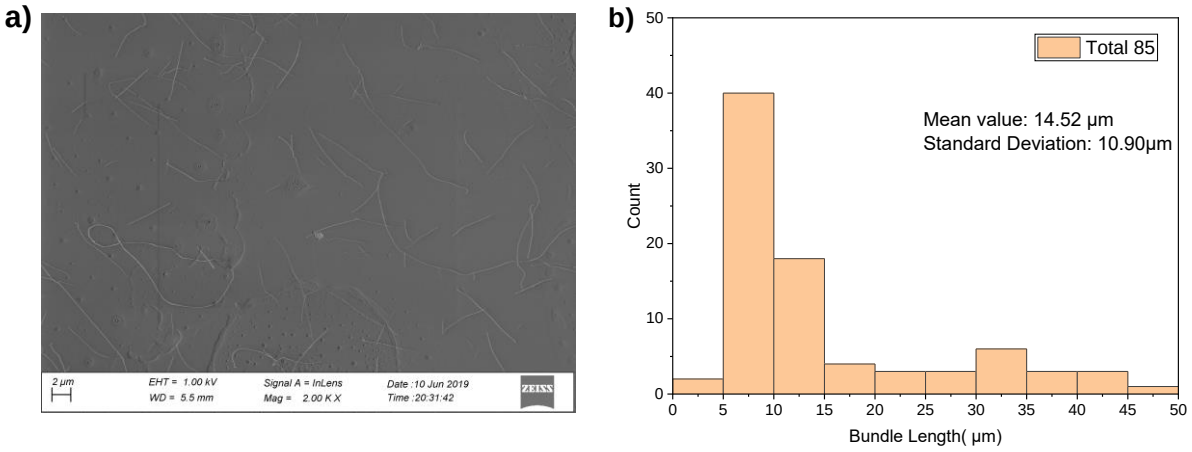

Figure 5.4.2. CNT bundle length distribution. a) A representative SEM image of CNT bundles deposited on silicon substrate by press-transfer method (20 s collection time on a 10 cm diameter filter). b) CNT bundle length distribution based on the statistics of 85 bundles.

6. Conclusion and Outlook

In this thesis, we studied the synthesis of high-quality CNTs with high yield via FC-CVD system. The CNT aerosol was directly deposited on the filter to fabricate the CNT-based TCFs. Methane (CH_4), the most stable hydrocarbon, is applied as a carbon source, ferrocene ($FeCp_2$) as catalyst precursor, sulfur (S) as a promoter, hydrogen (H_2) and nitrogen (N_2) as a carrier gas. Specially, the cartridges of $FeCp_2$ and sulfur were heated up for the high yield of CNT. The specific synthesis parameters were optimized to improve the yield and optoelectronic performance of CNT TCFs.

Firstly, the $FeCp_2$ cartridge was set at 45 °C where the saturated vapor pressure of $FeCp_2$ is around 6 times higher than that at 25 °C. The various growth parameters were optimized with respect to the yield and optoelectronic performance of TCFs. The CNT TCFs with a low sheet resistance of 75 Ω/sq at 90 T% was obtained with a super-high yield of 4 min collection on a 4.7 cm diameter filter. For this result, the specific synthetic conditions were a reactor temperature of 1100 °C, H_2 of 70 sccm, the total gas flow of 400 sccm, CH_4 of 8 sccm, and a molar ratio of Fe to S around 4.

To further improve the optoelectronic performance of TCFs, we reduced the CNT yield in a reasonable range via tuning the temperature of $FeCp_2$. The motivation came from that the low concentration of CNT aerosol can effectively reduce the probability of collision in the FCCVD synthesis process. And then long CNT bundles with small diameters can be obtained and this specific morphology can contribute to the high electrical conductivity of CNT TCFs. These results of lower yield-higher conductivity have been verified in the SWCNT-FCCVD system with CO, C_2H_4, and C_2H_6O as carbon source. Here, we studied the CNTs yield and TCFs performance at the $FeCp_2$ temperature of 45 °C, 40 °C, 35 °C and 30 °C with the constant Fe: S ratio of 4. The yield significantly decreases with low $FeCp_2$ temperature. However, the highest conductivity of CNT films was fabricated at $FeCp_2$ temperature of 40 °C. This CNT TCFs have a sheet resistance of 59 Ω/sq at 90 T% with 10 min collection on a 4.7 cm diameter filter. It is worth mentioning that the yield of CH_4-based CNT film at 40 °C of $FeCp_2$ is much higher than those of other SWCNT films, e.g. 20 times of CO-based SWCNT films with 86.8 Ω/sq at 90 T%, 150 times of C_2H_4-based SWCNT films with 51 Ω/sq at 90 T% and 10 times of C_2H_6O-based SWCNT films with 78 Ω/sq at 90 T%.

In this high-yield CNT FCCVD system, we found a distinctive result of the performance-yield relationship that the film conductivity is not monotonically reduced, but first improved and then declined with yield increase. To understand this result, we applied TEM and SEM to analyze the morphology of CNTs produced with $FeCp_2$ temperature of 40 °C. Surprisingly, we found both SWCNTs and DWCNTs simultaneously produced in this high-yield FCCVD system. Wherein, the proportion of DWCNTs with a diameter of 3.5-6 nm is up to 80%. SWCNTs with small diameter prefer bundling. The bundle diameter estimated at 8.3 nm and 35% of the CNTs are individual. Considering the high proportion of large-diameter DWCNTs, these bundles with a mean diameter of 8.3 nm are still quite ‘small’. Moreover, the mean length of these bundles is around 14.52 μm, which is similar to that from C_2H_4- FCCVD system.

These high-yield CNT TCFs with excellent conductivity produced via FCCVD have the potential to replace ITO in touch sensors, OLEDs and also the next generation electronics. The results, especially the large diameter CNT TCFs overcoming the yield-performance, are

valuable in the fields of both fundamental sciences of CNT synthesis and industrial applications of CNT TCFs. However, future research should be carried out to further understand these phenomena and improve the CNT TCFs conductivity, for example,

1. The relationship between CNT diameter, wall number, and catalyst size, chemical composition

2. Decouple catalyst nucleation with CNT synthesis to directly produce individual SWCNTs with a super-large diameter (over 3 nm)

3. Improve the CNT growth speed for super-long CNT synthesis

4. How the CNT diameter affects the junction resistances in CNT networks, which can be studied with the help of conductive atomic force microscopy.

References

[1] S. Iijima, Helical microtubules of graphitic carbon, Nature. (1991). https://doi.org/10.1038/354056a0.

[2] M.S.D. Ado Jorio, Gene Dresselhaus, Carbon nanotubes: Advanced topics in the synthesis, structure, properties and applications, 2008. https://doi.org/10.1016/s1369-7021(08)70021-x.

[3] S. Muhl, R. Aguilar Osorio, U.A. Martínez Huitle, Transparent conductive carbon nanotube films, Rev. Mex. Fis. 63 (2014) 439–447. https://doi.org/10.1126/science.1101243.

[4] Q. Cao, H.S. Kim, N. Pimparkar, J.P. Kulkarni, C. Wang, M. Shim, K. Roy, M.A. Alam, J.A. Rogers, Medium-scale carbon nanotube thin-film integrated circuits on flexible plastic substrates, Nature. (2008). https://doi.org/10.1038/nature07110.

[5] Q. Cao, J.A. Rogers, Ultrathin films of single-walled carbon nanotubes for electronics and sensors: A review of fundamental and applied aspects, Adv. Mater. (2009). https://doi.org/10.1002/adma.200801995.

[6] Y. Zhou, R. Azumi, Carbon nanotube based transparent conductive films: progress, challenges, and perspectives, Sci. Technol. Adv. Mater. (2016). https://doi.org/10.1080/14686996.2016.1214526.

[7] S. Iijima, T. Ichihashi, Single-shell carbon nanotubes of 1-nm diameter, Nature. (1993). https://doi.org/10.1038/363603a0.

[8] T. Guo, P. Nikolaev, A. Thess, D.T. Colbert, R.E. Smalley, Catalytic growth of single-walled manotubes by laser vaporization, Chem. Phys. Lett. (1995). https://doi.org/10.1016/0009-2614(95)00825-O.

[9] H. Dai, A.G. Rinzler, P. Nikolaev, A. Thess, D.T. Colbert, R.E. Smalley, Single-wall nanotubes produced by metal-catalyzed disproportionation of carbon monoxide, Chem. Phys. Lett. (1996). https://doi.org/10.1016/0009-2614(96)00862-7.

[10] P. Nikolaev, M.J. Bronikowski, R.K. Bradley, F. Rohmund, D.T. Colbert, K.A. Smith, R.E. Smalley, Gas-phase catalytic growth of single-walled carbon nanotubes from carbon monoxide, Chem. Phys. Lett. (1999). https://doi.org/10.1016/S0009-2614(99)01029-5.

[11] A. Moisala, A.G. Nasibulin, D.P. Brown, H. Jiang, L. Khriachtchev, E.I. Kauppinen, Single-walled carbon nanotube synthesis using ferrocene and iron pentacarbonyl in a laminar flow reactor, Chem. Eng. Sci. (2006). https://doi.org/10.1016/j.ces.2006.02.020.

[12] H.M. Cheng, F. Li, G. Su, H.Y. Pan, L.L. He, X. Sun, M.S. Dresselhaus, Large-scale and low-cost synthesis of single-walled carbon nanotubes by the catalytic pyrolysis of hydrocarbons, Appl. Phys. Lett. (1998). https://doi.org/10.1063/1.121624.

[13] Y. Liao, A. Hussain, P. Laiho, Q. Zhang, Y. Tian, N. Wei, E.X. Ding, S.A. Khan, N.N. Nguyen, S. Ahmad, E.I. Kauppinen, Tuning Geometry of SWCNTs by CO2 in Floating Catalyst CVD for High-Performance Transparent Conductive Films, Adv. Mater. Interfaces. 5 (2018) 1–10. https://doi.org/10.1002/admi.201801209.

[14] A. Hussain, Y. Liao, Q. Zhang, E.X. Ding, P. Laiho, S. Ahmad, N. Wei, Y. Tian, H. Jiang, E.I. Kauppinen, Floating catalyst CVD synthesis of single walled carbon nanotubes from ethylene for high performance transparent electrodes, Nanoscale. (2018). https://doi.org/10.1039/c8nr00716k.

[15] E.X. Ding, Q. Zhang, N. Wei, A.T. Khan, E.I. Kauppinen, High-performance single-walled carbon nanotube transparent conducting film fabricated by using low feeding rate of ethanol solution, R. Soc. Open Sci. 5 (2018). https://doi.org/10.1098/rsos.180392.

[16] R. Saito, G. Dresselhaus, M.S. Dresselhaus, Physical Properties of Carbon Nanotubes, 1998. https://doi.org/10.1142/p080.

[17] T. Dürkop, S.A. Getty, E. Cobas, M.S. Fuhrer, Extraordinary Mobility in Semiconducting Carbon Nanotubes, Nano Lett. (2004). https://doi.org/10.1021/nl034841q.

[18] J. Low, S. Cao, J. Yu, S. Wageh, Two-dimensional layered composite photocatalysts, Chem. Commun. (2014). https://doi.org/10.1039/c4cc02553a.

[19] A. Kaskela, Transparent, conductive and flexible single-walled carbon nanotube films, n.d.

[20] R. Saito, G. Dresselhaus, Trigonal warping effect of carbon nanotubes, Phys. Rev. B - Condens. Matter Mater. Phys. (2000). https://doi.org/10.1103/PhysRevB.61.2981.

[21] P.R. Wallace, The band theory of graphite, Phys. Rev. (1947). https://doi.org/10.1103/PhysRev.71.622.

[22] R. Saito, M. Fujita, G. Dresselhaus, M.S. Dresselhaus, Electronic structure of chiral graphene tubules, Appl. Phys. Lett. (1992). https://doi.org/10.1063/1.107080.

[23] R. Saito, M. Fujita, G. Dresselhaus, M.S. Dresselhaus, Electronic structure of graphene tubules based on C60, Phys. Rev. B. (1992). https://doi.org/10.1103/PhysRevB.46.1804.

[24] Y. Liao, Carbon dioxide-assisted synthesis of single-walled carbon nanotubes and their thin film properties, Dep. Appl. Physics, Dr. Philos. Aalto Univ. Espoo. (2019). https://aaltodoc.aalto.fi/handle/123456789/40231.

[25] Y.K. H.kataura, Optical properties of single-wall carbon nanotubes, Synth. Met. 103 (1999). https://doi.org/10.1016/S0379-6779(98)00278-1.

[26] X. Liu, T. Pichler, T. Pichler, M. Knupfer, M.S. Golden, J. Fink, H. Kataura, Y. Achiba, Detailed analysis of the mean diameter and diameter distribution of single-wall carbon nanotubes from their optical response, Phys. Rev. B - Condens. Matter Mater. Phys. (2002). https://doi.org/10.1103/PhysRevB.66.045411.

[27] M.S. Dresselhaus, G. Dresselhaus, R. Saito, A. Jorio, Raman spectroscopy of carbon nanotubes, Phys. Rep. (2005). https://doi.org/10.1016/j.physrep.2004.10.006.

[28] P.T. Araujo, S.K. Doorn, S. Kilina, S. Tretiak, E. Einarsson, S. Maruyama, H. Chacham, M.A. Pimenta, A. Jorio, Third and fourth optical transitions in semiconducting carbon nanotubes, Phys. Rev. Lett. (2007). https://doi.org/10.1103/PhysRevLett.98.067401.

[29] M. Ãu, Synthesis and Characterization of Vertically Aligned Single-Walled Carbon Nanotubes, Mech. Eng. (2006).

[30] M.S. Dresselhaus, P.C. Eklund, Phonons in carbon nanotubes, Adv. Phys. (2000). https://doi.org/10.1080/000187300413184.

[31] D.S. Bethune, C.H. Klang, M.S. De Vries, G. Gorman, R. Savoy, J. Vazquez, R. Beyers, Cobalt-catalysed growth of carbon nanotubes with single-atomic-layer walls, Nature. (1993). https://doi.org/10.1038/363605a0.

[32] P.M. Ajayan, J.M. Lambert, P. Bernier, L. Barbedette, C. Colliex, J.M. Planeix, Growth morphologies during cobalt-catalyzed single-shell carbon nanotube synthesis, Chem. Phys. Lett. (1993). https://doi.org/10.1016/0009-2614(93)85711-V.

[33] H. Fan, L. Wang, K. Zhao, N. Li, Z. Shi, Z. Ge, Z. Jin, Fabrication, mechanical properties, and biocompatibility of graphene-reinforced chitosan composites, Biomacromolecules. (2010). https://doi.org/10.1021/bm100470q.

[34] B. Chen, S. Inoue, Y. Ando, Raman spectroscopic and thermogravimetric studies of high-crystallinity SWNTs synthesized by FH-arc discharge method, Diam. Relat. Mater. (2009). https://doi.org/10.1016/j.diamond.2009.01.026.

[35] S. Seraphin, D. Zhou, J. Jiao, M.A. Minke, S. Wang, T. Yadav, J.C. Withers, Catalytic role of nickel, palladium, and platinum in the formation of carbon nanoclusters, Chem. Phys. Lett. (1994). https://doi.org/10.1016/0009-2614(93)E1376-R.

[36] Y. Saito, M. Okuda, T. Koyama, Carbon nanocapsules and single-wall nanotubes formed by arc evaporation, Surf. Rev. Lett. (1996). https://doi.org/10.1142/S0218625X96001558.

[37] Y. Saito, K. Nishikubo, K. Kawabata, T. Matsumoto, Carbon nanocapsules and single-layered nanotubes produced with platinum-group metals (Ru, Rh, Pd, Os, Ir, Pt) by arc discharge, J. Appl. Phys. (1996). https://doi.org/10.1063/1.363166.

[38] A.P. Bolshakov, S.A. Uglov, A. V. Saveliev, V.I. Konov, A.A. Gorbunov, W. Pompe, A. Graff, A novel CW laser-powder method of carbon single-wall nanotubes production, Diam. Relat. Mater. (2002). https://doi.org/10.1016/S0925-9635(01)00641-0.

[39] T. Ikegami, F. Nakanishi, M. Uchiyama, K. Ebihara, Optical measurement in carbon nanotubes formation by pulsed laser ablation, in: Thin Solid Films, 2004. https://doi.org/10.1016/j.tsf.2003.12.033.

[40] L.L. Lebel, B. Aissa, M.A. El Khakani, D. Therriault, Preparation and mechanical characterization of laser ablated single-walled carbon-nanotubes/polyurethane nanocomposite microbeams, Compos. Sci. Technol. 70 (2010) 518–524. https://doi.org/10.1016/j.compscitech.2009.12.004.

[41] R.T.K. Baker, M.A. Barber, P.S. Harris, F.S. Feates, R.J. Waite, Nucleation and growth of carbon deposits from the nickel catalyzed decomposition of acetylene, J. Catal. (1972). https://doi.org/10.1016/0021-9517(72)90032-2.

[42] J. Gavillet, A. Loiseau, C. Journet, F. Willaime, F. Ducastelle, J.C. Charlier, Root-growth mechanism for single-wall carbon nanotubes, Phys. Rev. Lett. (2001). https://doi.org/10.1103/PhysRevLett.87.275504.

[43] S. Huang, X. Cai, J. Liu, Growth of millimeter-long and horizontally aligned single-walled carbon nanotubes on flat substrates, J. Am. Chem. Soc. (2003). https://doi.org/10.1021/ja034475c.

[44] K. Hata, D.N. Futaba, K. Mizuno, T. Namai, M. Yumura, S. Iijima, Water-assisted highly efficient synthesis of impurity-free single-walled carbon nanotubes, Science (80-.). (2004). https://doi.org/10.1126/science.1104962.

[45] C. Feng, K. Liu, J.S. Wu, L. Liu, J.S. Cheng, Y. Zhang, Y. Sun, Q. Li, S. Fan, K. Jiang, Flexible, stretchable, transparent conducting films made from superaligned carbon nanotubes, Adv. Funct. Mater. (2010). https://doi.org/10.1002/adfm.200901960.

[46] M.J. Bronikowski, P.A. Willis, D.T. Colbert, K.A. Smith, R.E. Smalley, Gas-phase production of carbon single-walled nanotubes from carbon monoxide via the HiPco process: A parametric study, J. Vac. Sci. Technol. A Vacuum, Surfaces, Film. (2001). https://doi.org/10.1116/1.1380721.

[47] W. Ma, L. Song, R. Yang, T. Zhang, Y. Zhao, L. Sun, Y. Ren, D. Liu, L. Liu, J. Shen, Z. Zhang, Y. Xiang, W. Zhou, S.S. Xie, Directly synthesized strong, highly conducting, transparent single-walled carbon nanotube films, Nano Lett. (2007). https://doi.org/10.1021/nl070915c.

[48] A. Kaskela, A.G. Nasibulin, M.Y. Timmermans, B. Aitchison, A. Papadimitratos, Y. Tian, Z. Zhu, H. Jiang, D.P. Brown, A. Zakhidov, E.I. Kauppinen, Aerosol-synthesized SWCNT networks with tunable conductivity and transparency by a dry transfer technique, Nano Lett. (2010). https://doi.org/10.1021/nl101680s.

[49] Q. Zhang, K. Li, Q. Fan, X. Xia, N. Zhang, Z. Xiao, W. Zhou, F. Yang, Y. Wang, H. Liu, W. Zhou, Performance improvement of continuous carbon nanotube fibers by acid treatment, Chinese Phys. B. (2017). https://doi.org/10.1088/1674-1056/26/2/028802.

[50] Y.L. Li, I.A. Kinloch, A.H. Windle, Direct Spinning of Carbon Nanotube Fibers from Chemical Vapor Deposition Synthesis, Science (80-.). (2004). https://doi.org/10.1126/science.1094982.

[51] X. Gui, A. Cao, J. Wei, H. Li, Y. Jia, Z. Li, L. Fan, K. Wang, H. Zhu, D. Wu, Soft, highly conductive nanotube sponges and composites with controlled compressibility, ACS Nano. (2010). https://doi.org/10.1021/nn100114d.

[52] E. Lamouroux, P. Serp, P. Kalck, Catalytic routes towards single wall carbon nanotubes, Catal. Rev. - Sci. Eng. (2007). https://doi.org/10.1080/01614940701313200.

[53] J.S. Barnard, C. Paukner, K.K. Koziol, The role of carbon precursor on carbon nanotube chirality in floating catalyst chemical vapour deposition, Nanoscale. (2016). https://doi.org/10.1039/c6nr03895f.

[54] A.G. Nasibulin, A. Moisala, D.P. Brown, H. Jiang, E.I. Kauppinen, A novel aerosol method for single walled carbon nanotube synthesis, Chem. Phys. Lett. (2005). https://doi.org/10.1016/j.cplett.2004.12.040.

[55] A. Moisala, A.G. Nasibulin, E.I. Kauppinen, The role of metal nanoparticles in the catalytic production of single-walled carbon nanotubes - A review, J. Phys. Condens. Matter. (2003). https://doi.org/10.1088/0953-8984/15/42/003.

[56] K. Mustonen, P. Laiho, A. Kaskela, Z. Zhu, O. Reynaud, N. Houbenov, Y. Tian, T. Susi, H. Jiang, A.G. Nasibulin, E.I. Kauppinen, Gas phase synthesis of non-bundled, small diameter single-walled carbon nanotubes with near-armchair chiralities, Appl. Phys. Lett. (2015). https://doi.org/10.1063/1.4926415.

[57] H.M. Cheng, F. Li, X. Sun, S.D.M. Brown, M.A. Pimenta, A. Marucci, G. Dresselhaus, M.S. Dresselhaus, Bulk morphology and diameter distribution of single-walled carbon nanotubes synthesized by catalytic decomposition of hydrocarbons, Chem. Phys. Lett. (1998). https://doi.org/10.1016/S0009-2614(98)00479-5.

[58] Y.L. Li, L.H. Zhang, X.H. Zhong, A.H. Windle, Synthesis of high purity single-walled carbon nanotubes from ethanol by catalytic gas flow CVD reactions, Nanotechnology. (2007). https://doi.org/10.1088/0957-4484/18/22/225604.

[59] Q. Zhang, N. Wei, P. Laiho, E.I. Kauppinen, Recent Developments in Single-Walled Carbon Nanotube Thin Films Fabricated by Dry Floating Catalyst Chemical Vapor Deposition, Top. Curr. Chem. (2017). https://doi.org/10.1007/s41061-017-0178-8.

[60] M. He, H. Jiang, E.I. Kauppinen, J. Lehtonen, Diameter and chiral angle distribution dependencies on the carbon precursors in surface-grown single-walled carbon nanotubes, Nanoscale. (2012). https://doi.org/10.1039/c2nr32276e.

[61] A.R. Harutyunyan, G. Chen, T.M. Paronyan, E.M. Pigos, O.A. Kuznetsov, K. Hewaparakrama, S.M. Kim, D. Zakharov, E.A. Stach, G.U. Sumanasekera, Preferential growth of single-walled carbon nanotubes with metallic conductivity, Science (80-.). (2009). https://doi.org/10.1126/science.1177599.

[62] J.J. Vilatela, A.H. Windle, Yarn-like carbon nanotube fibers, Adv. Mater. (2010). https://doi.org/10.1002/adma.201002131.

[63] A.G. Nasibulin, D.P. Brown, P. Queipo, D. Gonzalez, H. Jiang, E.I. Kauppinen, An essential role of CO2 and H2O during single-walled CNT synthesis from carbon monoxide, Chem. Phys. Lett. (2006). https://doi.org/10.1016/j.cplett.2005.10.022.

[64] A. Kaskela, P. Laiho, N. Fukaya, K. Mustonen, T. Susi, H. Jiang, N. Houbenov, Y. Ohno, E.I. Kauppinen, Highly individual SWCNTs for high performance thin film electronics, Carbon N. Y. (2016).

https://doi.org/10.1016/j.carbon.2016.02.099.

[65] D.S. Hecht, L. Hu, G. Irvin, Emerging transparent electrodes based on thin films of carbon nanotubes, graphene, and metallic nanostructures, Adv. Mater. (2011). https://doi.org/10.1002/adma.201003188.

[66] M. Duta, M. Anastasescu, J.M. Calderon-Moreno, L. Predoana, S. Preda, M. Nicolescu, H. Stroescu, V. Bratan, I. Dascalu, E. Aperathitis, M. Modreanu, M. Zaharescu, M. Gartner, Sol–gel versus sputtering indium tin oxide films as transparent conducting oxide materials, J. Mater. Sci. Mater. Electron. (2016). https://doi.org/10.1007/s10854-016-4375-y.

[67] C.Y. Chen, W.K. Lee, Y.J. Chen, C.Y. Lu, H.Y. Lin, C.C. Wu, Enhancing Optical Out-Coupling of Organic Light-Emitting Devices with Nanostructured Composite Electrodes Consisting of Indium Tin Oxide Nanomesh and Conducting Polymer, Adv. Mater. (2015). https://doi.org/10.1002/adma.201502516.

[68] A. Mora, K.A. Khan, T. El Sayed, Crack density and electrical resistance in indium-tin-oxide/polymer thin films under cyclic loading, Electron. Mater. Lett. 10 (2014) 1033–1037. https://doi.org/10.1007/s13391-014-3321-5.

[69] Z. Chen, W. Li, R. Li, Y. Zhang, G. Xu, H. Cheng, Fabrication of highly transparent and conductive indium-tin oxide thin films with a high figure of merit via solution processing, Langmuir. (2013). https://doi.org/10.1021/la4033282.

[70] Y. Sun, B. Gates, B. Mayers, Y. Xia, Crystalline Silver Nanowires by Soft Solution Processing, Nano Lett. (2002). https://doi.org/10.1021/nl010093y.

[71] L. Hu, H.S. Kim, J.Y. Lee, P. Peumans, Y. Cui, Scalable coating and properties of transparent, flexible, silver nanowire electrodes, ACS Nano. (2010). https://doi.org/10.1021/nn1005232.

[72] S. De, T.M. Higgins, P.E. Lyons, E.M. Doherty, P.N. Nirmalraj, W.J. Blau, J.J. Boland, J.N. Coleman, Silver nanowire networks as flexible, transparent, conducting films: Extremely high DC to optical conductivity ratios, ACS Nano. (2009). https://doi.org/10.1021/nn900348c.

[73] S. Bae, H. Kim, Y. Lee, X. Xu, J.S. Park, Y. Zheng, J. Balakrishnan, T. Lei, H. Ri Kim, Y. Il Song, Y.J. Kim, K.S. Kim, B. Özyilmaz, J.H. Ahn, B.H. Hong, S. Iijima, Roll-to-roll production of 30-inch graphene films for transparent electrodes, Nat. Nanotechnol. (2010). https://doi.org/10.1038/nnano.2010.132.

[74] X. Li, Y. Zhu, W. Cai, M. Borysiak, B. Han, D. Chen, R.D. Piner, L. Colomba, R.S. Ruoff, Transfer of large-area graphene films for high-performance transparent conductive electrodes, Nano Lett. (2009). https://doi.org/10.1021/nl902623y.

[75] B. Dan, G.C. Irvin, M. Pasquali, Continuous and scalable fabrication of transparent conducting carbon nanotube films, ACS Nano. (2009). https://doi.org/10.1021/nn8008307.

[76] S. Jiang, P.X. Hou, M.L. Chen, B.W. Wang, D.M. Sun, D.M. Tang, Q. Jin, Q.X. Guo, D.D. Zhang, J.H. Du, K.P. Tai, J. Tan, E.I. Kauppinen, C. Liu, H.M. Cheng, Ultrahigh-performance transparent conductive films of carbon-welded isolated single-wall carbon nanotubes, Sci. Adv. (2018). https://doi.org/10.1126/sciadv.aap9264.

[77] S. De, J.N. Coleman, Are there fundamental limitations on the sheet resistance and transmittance of thin graphene films?, ACS Nano. (2010). https://doi.org/10.1021/nn100343f.

[78] A. Kasry, M.A. Kuroda, G.J. Martyna, G.S. Tulevski, A.A. Bol, Chemical doping of large-area stacked graphene films for use as transparent, conducting electrodes, ACS Nano. (2010). https://doi.org/10.1021/nn100508g.

[79] S.Y. Jeong, S.H. Kim, J.T. Han, H.J. Jeong, S. Yang, G.W. Lee, High-performance transparent conductive films using rheologically derived reduced graphene oxide, ACS Nano. (2011). https://doi.org/10.1021/nn102017f.

[80] K.H. Park, B.H. Kim, S.H. Song, J. Kwon, B.S. Kong, K. Kang, S. Jeon, Exfoliation of non-oxidized graphene flakes for scalable conductive film, Nano Lett. (2012). https://doi.org/10.1021/nl3004732.

[81] S. Pang, Y. Hernandez, X. Feng, K. Müllen, Graphene as transparent electrode material for organic electronics, Adv. Mater. (2011). https://doi.org/10.1002/adma.201100304.

[82] Y. Lee, J.H. Ahn, Graphene-based transparent conductive films, Nano. (2013). https://doi.org/10.1142/S1793292013300016.

[83] X. Tian, M.L. Moser, A. Pekker, S. Sarkar, J. Ramirez, E. Bekyarova, M.E. Itkis, R.C. Haddon, Effect of atomic interconnects on percolation in single-walled carbon nanotube thin film networks, Nano Lett. (2014). https://doi.org/10.1021/nl501212u.

[84] E.X. Ding, Q. Zhang, N. Wei, A.T. Khan, E.I. Kauppinen, High-performance single-walled carbon nanotube transparent conducting film fabricated by using low feeding rate of ethanol solution, R. Soc. Open Sci. (2018). https://doi.org/10.1098/rsos.180392.

[85] A. Znidarsic, A. Kaskela, P. Laiho, M. Gaberscek, Y. Ohno, A.G. Nasibulin, E.I. Kauppinen, A. Hassanien, Spatially resolved transport properties of pristine and doped single-walled carbon nanotube networks, J. Phys. Chem. C. (2013). https://doi.org/10.1021/jp403983y.

[86] M. Stadermann, S.J. Papadakis, M.R. Falvo, J. Novak, E. Snow, Q. Fu, J. Liu, Y. Fridman, J.J. Boland, R. Superfine, S. Washburn, Nanoscale study of conduction through carbon nanotube networks, Phys. Rev. B - Condens. Matter Mater. Phys. (2004). https://doi.org/10.1103/PhysRevB.69.201402.

[87] D. Simien, J.A. Fagan, W. Luo, J.F. Douglas, K. Migler, J. Obrzut, Influence of nanotube length on the optical and conductivity properties of thin single-wall carbon nanotube networks, ACS Nano. (2008). https://doi.org/10.1021/nn800376x.

[88] D. Hecht, L. Hu, G. Grüner, Conductivity scaling with bundle length and diameter in single walled carbon nanotube networks, Appl. Phys. Lett. (2006). https://doi.org/10.1063/1.2356999.

[89] S. Li, Z. Yu, C. Rutherglen, P.J. Burke, Electrical properties of 0.4 cm long single-walled carbon nanotubes, Nano Lett. (2004). https://doi.org/10.1021/nl048687z.

[90] Z. Yao, C.L. Kane, C. Dekker, High-field electrical transport in single-wall carbon nanotubes, Phys. Rev. Lett. (2000). https://doi.org/10.1103/PhysRevLett.84.2941.

[91] P. Laiho, M. Rafiee, Y. Liao, A. Hussain, E.X. Ding, E.I. Kauppinen, Wafer-Scale Thermophoretic Dry Deposition of Single-Walled Carbon Nanotube Thin Films, ACS Omega. (2018). https://doi.org/10.1021/acsomega.7b01869.

[92] D.S. Hecht, A.M. Heintz, R. Lee, L. Hu, B. Moore, C. Cucksey, S. Risser, High conductivity transparent carbon nanotube films deposited from superacid, Nanotechnology. (2011). https://doi.org/10.1088/0957-4484/22/7/075201.

[93] E.X. Ding, H. Jiang, Q. Zhang, Y. Tian, P. Laiho, A. Hussain, Y. Liao, N. Wei, E.I. Kauppinen, Highly conductive and transparent single-walled carbon nanotube thin films from ethanol by floating catalyst chemical vapor deposition, Nanoscale. 9 (2017) 17601–17609. https://doi.org/10.1039/c7nr05554d.

[94] I. V. Anoshkin, A.G. Nasibulin, Y. Tian, B. Liu, H. Jiang, E.I. Kauppinen, Hybrid carbon source for single-walled carbon nanotube synthesis by aerosol CVD method, Carbon N. Y. (2014). https://doi.org/10.1016/j.carbon.2014.06.057.

[95] A.G. Nasibulin, A. Kaskela, K. Mustonen, A.S. Anisimov, V. Ruiz, S. Kivistö, S. Rackauskas, M.Y. Timmermans, M. Pudas, B. Aitchison, M. Kauppinen, D.P. Brown, O.G. Okhotnikov, E.I. Kauppinen, Multifunctional free-standing single-walled carbon nanotube films, ACS Nano. (2011). https://doi.org/10.1021/nn200338r.

[96] P. Laiho, K. Mustonen, Y. Ohno, S. Maruyama, E.I. Kauppinen, Dry and Direct Deposition of Aerosol-Synthesized Single-Walled Carbon Nanotubes by Thermophoresis, ACS Appl. Mater. Interfaces. (2017). https://doi.org/10.1021/acsami.7b03151.

[97] Y. Tian, S. Ahmad, E.I. Kauppinen, PHYS-E0411 Advanced Physics Single-walled Carbon Nanotubes, (2018).

[98] K. Vajanto, PHYS-E0525_2016_Lecture_6_SEM, (2016).

[99] F.Y. Zhu, Q.Q. Wang, X.S. Zhang, W. Hu, X. Zhao, H.X. Zhang, 3D nanostructure reconstruction based on the SEM imaging principle, and applications, Nanotechnology. 25 (2014). https://doi.org/10.1088/0957-4484/25/18/185705.

[100] L.B. Valdes, Resistivity Measurements on Germanium for Transistors, Proc. IRE. (1954). https://doi.org/10.1109/JRPROC.1954.274680.

[101] K.K. Kim, S.M. Yoon, H.K. Park, H.J. Shin, S.M. Kim, J.J. Bae, Y. Cui, J.M. Kim, J.Y. Choi, Y.H. Lee, Doping strategy of carbon nanotubes with redox chemistry, New J. Chem. (2010). https://doi.org/10.1039/c0nj00138d.

[102] K.K. Ki, J.B. Jung, K.P. Hyeon, M.K. Soo, H.Z. Geng, A.P. Kyung, H.J. Shin, S.M. Yoon, A. Benayad, J.Y. Choi, H.L. Young, Fermi level engineering of single-walled carbon nanotubes by AuCl 3 doping, J. Am. Chem. Soc. (2008). https://doi.org/10.1021/ja8038689.